J. Fluid Mech. (2001), *vol.* 445, *pp.* 377–411. © 2001 Cambridge University Press
DOI: 10.1017/S0022112001005857 Printed in the United Kingdom

Coupled pulsation and translation of two gas bubbles in a liquid

By ANTHONY HARKIN[1]†, TASSO J. KAPER[1]† AND ALI NADIM[2]†

[1]Department of Mathematics, Boston University, Boston, MA 02215, USA

[2]Department of Aerospace and Mechanical Engineering, Boston University, Boston, MA 02215, USA

(Received 23 December 2000 and in revised form 25 May 2001)

We present and analyse a model for the spherical pulsations and translational motions of a pair of interacting gas bubbles in an incompressible liquid. The model is derived rigorously in the context of potential flow theory and contains all terms up to and including fourth order in the inverse separation distance between the bubbles. We use this model to study the cases of both weak and moderate applied acoustic forcing. For weak acoustic forcing, the radial pulsations of the bubbles are weakly coupled, which allows us to obtain a nonlinear time-averaged model for the relative distance between the bubbles. The two parameters of the time-averaged model classify four different dynamical regimes of relative translational motion, two of which correspond to the attraction and repulsion of classical secondary Bjerknes theory. Also predicted is a pattern in which the bubbles exhibit stable, time-periodic translational oscillations along the line connecting their centres, and another pattern in which there is an unstable separation distance such that bubble pairs can either attract or repel each other depending on whether their initial separation distance is smaller or larger than this value. Moreover, it is shown that the full governing equations possess the dynamics predicted by the time-averaged model. We also study the case of moderate-amplitude acoustic forcing, in which the bubble pulsations are more strongly coupled to each other and bubble translation also affects the radial pulsations. Here, radial harmonics and nonlinear phase shifting play a significant role, as bubble pairs near resonances are observed to translate in patterns opposite to those predicted by classical secondary Bjerknes theory. In this work, dynamical systems techniques and the method of averaging are the primary mathematical methods that are employed.

1. Introduction

The mutual force between two pulsating gas bubbles in a liquid was first studied by V. F. K. Bjerknes (1906) and C. A. Bjerknes (1915). They observed that this mutual force, known today as the secondary Bjerknes force, caused the bubbles to either attract or repel each other depending upon whether the bubble pulsations were in phase or out of phase, respectively. In particular, when the frequency of an applied acoustic field driving the pulsations was greater than or less than the natural oscillation frequencies of both bubbles, then the bubbles were found to pulsate in phase and attract, whereas if the driving frequency was in between the two natural

† Also a member of the Center for BioDynamics, Boston University, Boston, MA 02215, USA.

frequencies, the bubbles would oscillate out of phase and repel each other. Moreover, the magnitude of the force between two bubbles, directed along the line connecting their centres, was found to be proportional to the inverse square of the distance between them.

In recent years, it has been observed that two interacting gas bubbles in a liquid can exhibit dynamics which are more complicated than the motions produced by the classical secondary Bjerknes force (Zabolotskaya 1984; Oguz & Prosperetti 1990; Doinikov & Zavtrak 1995; Mettin *et al.* 1997; Barbat, Ashgriz & Liu 1999; Harkin 2001). Numerical simulations of a nonlinear model of two pulsating and translating bubbles (Oguz & Prosperetti 1990) demonstrate that increasing the acoustic forcing can even reverse the direction of the force between two bubbles from that predicted by the classical secondary Bjerknes force. Similar numerical results are also observed in a model with fixed bubble centres (Mettin *et al.* 1997). In addition, two bubbles in an incompressible liquid can undergo stable, periodic translational motion as has been observed in the recent experiments of Barbat *et al.* (1999). Examination of the normal modes of the linearized equations for fixed-centre bubbles (Zabolotskaya 1984) shows that the natural frequencies increase with decreasing separation distance. Hence, when the driving frequency is greater than both natural frequencies, the force may switch from attractive to repulsive, since the driving frequency actually lies in between the natural frequencies once the separation distance has become small enough. Finally, two bubbles can maintain a fixed (small) separation distance, forming a stable bound pair due to the second-harmonic component of the interaction force (Doinikov 1999), which is strong for small separation distances. The underlying mechanisms governing many of these new types of two-bubble dynamics are not well understood. Moreover, the full range of possible dynamics for two interacting bubbles is not yet known.

In this work, we endeavour to shed new light on these questions by presenting a joint analytical and numerical investigation of two interacting spherical gas bubbles in a liquid to which a sound field is applied. We begin by deriving the potential for this flow field with interaction terms up to and including fourth order in inverse powers of the separation distance, see § 2 and Appendix A. Five coupled nonlinear ordinary differential equations for the radial pulsations of the bubbles and for their translations are then derived from this potential in § 3, that are also accurate up to and including fourth order. Our analysis and simulations of the governing equations then lead to a classification of many of the patterns of motion for both weak and moderate applied acoustic forcing.

In the case of a weak applied sound field, the analysis predicts the existence of four distinct dynamical regimes. The different observed dynamics are: (1) bubble pairs that execute periodic translational motion about an equilibrium separation distance, (2) bubble pairs that either attract (if they start sufficiently close) or repel (when they start farther apart), due to the presence of an unstable equilibrium separation distance, (3) bubble pairs that always attract (and collide), and (4) bubble pairs that always repel; see §§ 4 and 5. Moreover, analysis of the final three regimes reveals that bubble pairs for which the initial translational velocity is not zero may exhibit the opposite dynamics over an initial transient period. For example, in the third regime, there may be an initial period in which the two bubbles move away from each other before they turn around and begin to move toward each other.

Two key parameters arise in the analysis of the weak forcing case in §§ 4 and 5. The four possible sign combinations of these parameters then give rise to the four dynamical regimes described above. Their signs depend on the equilibrium radii of the bubbles, their natural frequencies, and the acoustic forcing frequency.

Most significantly, time-periodic translations of the bubble pair (first regime) are found to occur when the driving frequency is greater than the natural frequencies of both bubbles. The second regime corresponds to the case in which the driving frequency is between the two natural frequencies but closer to the smaller one. Then, the remaining two (Bjerknes) regimes correspond to the cases in which the driving frequency is less than both natural frequencies (regime three), and in between but closer to the larger frequency (regime four), respectively. This classification can be thought of as an enhanced Bjerknes theory, which holds when the translational velocities of the bubbles have magnitudes on the order of the inverse square of the separation distance.

Next, we study the case of a moderately strong driving sound field in § 6. We identify those terms from the full two-bubble model that are negligible under weak forcing, but become significant as the forcing amplitude increases. In particular, the translational velocities become larger, and hence so do the coupling terms in all of the equations of motion. The four distinct types of dynamics found with weak forcing are still observed to occur; however the boundaries of these regimes are significantly altered. In particular, qualitatively different types of dynamics emerge due to resonances between the volume oscillations of the bubbles and the driving sound field. In large regions of parameter and phase space, it is observed that bubble pairs that attract when weakly forced can be made to repel when strongly forced, and vice versa. For example, for large forcing there is a two-to-one resonance region in which repulsion is observed that emerges in that part of the parameter space corresponding to bubble attraction with weak forcing. Moreover, we demonstrate that nonlinear phase-locking of the bubble pulsations is a mechanism through which the mutual force between two bubbles can reverse direction. This aspect of our work therefore explains and quantifies the numerical observations made in Oguz & Prosperetti (1990). Moreover, since our model allows both bubbles to translate, the bifurcation diagrams we present extend the results of Mettin *et al.* (1997) for stationary bubbles in weakly compressible liquids.

The results of this study are summarized and further discussed in § 7. There we also explain in more detail how our work relates to recent analytical models and experimental results for spherically symmetric bubbles that are sufficiently far apart. For example, our classification of the weak forcing case resembles the classification developed in Barbat *et al.* (1999), but the analysis and the two key parameters used to classify bubble motions in that work differ from the analysis and parameters derived in this study.

Many other two-bubble studies have appeared in the literature. The effects of damping have been studied in Doinikov (1997*b*). Weak liquid compressibility has been shown to lead to a dampening of the secondary Bjerknes force (Fujikawa & Takahira 1986) in a model based on the potentials for two isolated bubbles and on the assumption of fixed bubble centres. Subsequent work of Takahira, Fujikawa & Akamatsu (1989) reports a difference between bubble responses to resonances caused by primary and secondary Bjerknes forces. Compressibility of the surrounding liquid also gives rise to two long-range forces (Doinikov & Zavtrak 1997) that become important when the wavelength of the incident sound field is so short as to be comparable to the bubble separation distance. These forces act along the direction of the line of centres and of the gradient of the incident acoustic field, and they can combine to create stable bound pairs in which the bubbles maintain a fixed separation distance. These forces are negligible in the present work, since we consider forcing fields with wavelengths significantly larger than the bubble separation distances.

Shape deformations, which we do not examine in the present work, have also been observed and analysed for different applied acoustic fields. In the case of two initially identical bubbles and a step change in the externally applied pressure field, typically either spherical-cap shapes or globally deformed bubbles are observed (Pelekasis 1991; Pelekasis & Tsamopoulos 1993*a*) in the attractive regime, leading to an eventual breakup of the bubbles. For oscillatory applied fields, Pelekasis (1991) and Pelekasis & Tsamopoulos (1993*b*) report agreement with the classical linear theory for low forcing amplitudes. By contrast, for oscillatory forcing with large amplitudes and with frequency in between the natural (volume) frequencies, they identify a subharmonic resonance at half the natural frequency of the bubble with smaller period that significantly alters the shape deformations and the interaction force.

1.1. *Classical secondary Bjerknes force*

Here, we briefly review the classical theory of the secondary Bjerknes force. Consider two spherical gas bubbles of radii $R_1(t)$ and $R_2(t)$ undergoing damped and driven radial pulsations in a liquid of density ρ, viscosity $\mu_{\rm vis}$, and ambient hydrostatic pressure p_0^∞. Suppose that the bubble centres are fixed and that the centre-to-centre distance between the bubbles is denoted by D. For large enough D, the pulsations of each bubble do not influence those of the other, so that the radial oscillations of each are governed by the well-known Rayleigh–Plesset equation (Plesset & Prosperetti 1977; Leal 1992; Leighton 1994):

$$R_j\ddot{R}_j + \tfrac{3}{2}\dot{R}_j^2 = \frac{1}{\rho}\left[\left(p_0^\infty + \frac{2\sigma}{R_{j0}}\right)\left(\frac{R_{j0}}{R_j}\right)^{3\kappa} - 4\mu\frac{\dot{R}_j}{R_j} - \frac{2\sigma}{R_j} - p_0^\infty + p_A\cos(\Omega t)\right], \quad j = 1, 2.$$

The radial pulsations of the bubbles are damped by thermal, viscous and radiative effects that are represented by the effective damping parameter $\mu = \mu_{\rm th} + \mu_{\rm vis} + \mu_{\rm rad}$. The equilibrium radius of bubble j is R_{j0}, the parameter σ denotes the surface tension of the bubble interface and κ is the polytropic exponent of the gas inside the bubbles, which is assumed to obey the ideal gas law. The pressure in the liquid far from the bubbles is taken to be $p_0^\infty - p_A\cos(\Omega t)$.

The radial pulsations of each bubble affect the pressure field in the vicinity of the other bubble. In the context of potential flow theory and for *fixed* separation distance D, the force on bubble 1 due to the pulsations of bubble 2 is given by

$$F_1(t) \approx -2\pi\rho\frac{R_1^2}{D^2}\frac{\mathrm{d}}{\mathrm{d}t}(R_1R_2^2\dot{R}_2). \tag{1.1}$$

The classical secondary Bjerknes force is the time-averaged force $\langle F_1(t)\rangle$ when both bubbles undergo small-amplitude radial pulsations $R_j(t) = R_{j0}[1+x_j(t)]$ with $|x_j| \ll 1$. In that case, the Rayleigh–Plesset equations can be linearized:

$$\ddot{x}_j + \zeta_j\dot{x}_j + \omega_{j0}^2 x_j = P_j\cos(\Omega t), \quad j = 1, 2,$$

where the parameters are given by

$$\omega_{j0}^2 = \frac{3\kappa p_0^\infty}{\rho R_{j0}^2} + \frac{2\sigma(3\kappa-1)}{\rho R_{j0}^3}, \qquad \zeta_j = \frac{4\mu}{\rho R_{j0}^2}, \qquad P_j = \frac{p_A}{\rho R_{j0}^2}, \tag{1.2}$$

and the natural oscillation frequency of a bubble, ω_{j0}, is known as the Minnaert frequency, see Minnaert (1933). The small-amplitude long-time solution of the Rayleigh–Plesset equation is

$$R_j(t) = R_{j0}[1 + \delta_j\cos(\Omega t + \psi_j)], \quad j = 1, 2, \tag{1.3}$$

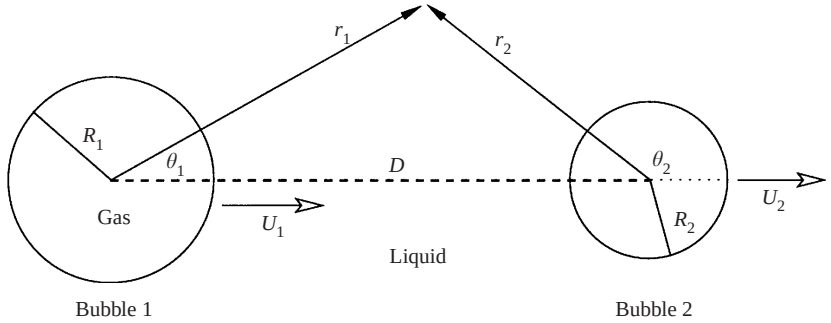

FIGURE 1. Schematic diagram for two pulsating and translating bubbles.

where

$$\delta_j = \frac{P_j}{\sqrt{(\omega_{10}^2 - \Omega^2)^2 + \Omega^2\zeta_j^2}} \qquad \text{and} \qquad \tan\psi_j = \frac{\Omega\zeta_j}{\Omega^2 - \omega_{10}^2}.$$

The classical expression for the secondary Bjerknes force follows directly from substituting (1.3) into (1.1) and averaging over one acoustic driving cycle:

$$\langle F_1(t)\rangle = \frac{2\pi\rho\Omega^2 R_{10}^3 R_{20}^3}{D^2}\delta_1\delta_2\cos(\psi_1 - \psi_2),$$

see Crum (1975). When the bubbles pulsate in phase, $\cos(\psi_1 - \psi_2)$ is positive, and the mutual force between the bubbles is attractive, whereas when the bubbles pulsate out of phase, $\cos(\psi_1 - \psi_2)$ is negative, and the mutual force is repulsive.

2. Velocity potential for two pulsating, translating bubbles

Allowing the bubble centres to move, we now consider two spherically pulsating gas bubbles immersed in an incompressible, irrotational fluid (figure 1). We assume that the bubbles remain spherical and that they only translate along their line of centres. Let $R_1(t)$ and $R_2(t)$ denote the time-dependent bubble radii, $U_1(t)$ and $U_2(t)$ the translation speeds of the bubble centres, and $D(t)$ the distance between the bubble centres, where $D(t) \gg R_1(t) + R_2(t)$. Local axisymmetric spherical coordinates, (r, θ), attached to and translating with each bubble centre are also defined as shown in figure 1.

The velocity potential, Φ, for the fluid flow velocity outside the bubbles, $\boldsymbol{u} = \nabla\Phi$, satisfies

$$\begin{aligned}
\Delta\Phi &= 0 && \text{on} && \{r_1 > R_1\}\bigcap\{r_2 > R_2\},\\
\nabla\Phi &\to \mathbf{0} && \text{as} && r_1, r_2 \to \infty,\\
\frac{\partial\Phi}{\partial n_1} &= \dot{R}_1 + U_1\cos\theta_1 && \text{on} && r_1 = R_1,\\
\frac{\partial\Phi}{\partial n_2} &= \dot{R}_2 + U_2\cos\theta_2 && \text{on} && r_2 = R_2,
\end{aligned}$$

where $\boldsymbol{n}$ is an outward unit normal to the bubble surface and $\partial/\partial n \equiv \boldsymbol{n}\cdot\nabla$. The velocity potential is determined by the method of images in Appendix A. In the local axisymmetric spherical coordinates of bubble 1 it is given by the following expansion

in powers of $1/D$:

$$\begin{aligned}\Phi(r_1,\theta_1) = &-\frac{R_1^2\dot{R}_1}{r_1} - \frac{U_1R_1^3}{2}\frac{\cos\theta_1}{r_1^2} - \frac{R_2^2\dot{R}_2}{D} - \frac{R_2^2\dot{R}_2P_1(\cos\theta_1)}{D^2}\left(r_1+\frac{R_1^3}{2r_1^2}\right) + \frac{U_2R_2^3}{2D^2}\\ &-\frac{R_2^2\dot{R}_2P_2(\cos\theta_1)}{D^3}\left(r_1^2+\frac{2R_1^5}{3r_1^3}\right) + \frac{U_2R_2^3P_1(\cos\theta_1)}{D^3}\left(r_1+\frac{R_1^3}{2r_1^2}\right)\\ &-\frac{R_2^2\dot{R}_2P_3(\cos\theta_1)}{D^4}\left(r_1^3+\frac{3R_1^7}{4r_1^4}\right) - \frac{R_1^3R_2^2\dot{R}_2}{2D^4}\\ &+\frac{U_2R_2^3P_2(\cos\theta_1)}{D^4}\left(\frac{3r_1^2}{2}+\frac{R_1^5}{r_1^3}\right) + O\left(\frac{1}{D^5}\right),\end{aligned} \tag{2.1}$$

where

$$P_0(x)=1, \qquad P_1(x)=x, \qquad P_2(x)=\tfrac{1}{2}(3x^2-1), \qquad P_3(x)=\tfrac{1}{2}(5x^3-3x)$$

are the first four Legendre polynomials. In the local axisymmetric spherical coordinates of bubble 2 the velocity potential is

$$\begin{aligned}\Phi(r_2,\theta_2) = &-\frac{R_2^2\dot{R}_2}{r_2} - \frac{U_2R_2^3}{2}\frac{\cos\theta_2}{r_2^2} - \frac{R_1^2\dot{R}_1}{D} + \frac{R_1^2\dot{R}_1P_1(\cos\theta_2)}{D^2}\left(r_2+\frac{R_2^3}{2r_2^2}\right) - \frac{U_1R_1^3}{2D^2}\\ &-\frac{R_1^2\dot{R}_1P_2(\cos\theta_2)}{D^3}\left(r_2^2+\frac{2R_2^5}{3r_2^3}\right) - \frac{U_1R_1^3P_1(\cos\theta_2)}{D^3}\left(r_2+\frac{R_2^3}{2r_2^2}\right)\\ &+\frac{R_1^2\dot{R}_1P_3(\cos\theta_2)}{D^4}\left(r_2^3+\frac{3R_2^7}{4r_2^4}\right) - \frac{R_2^3R_1^2\dot{R}_1}{2D^4}\\ &-\frac{U_1R_1^3P_2(\cos\theta_2)}{D^4}\left(\frac{3r_2^2}{2}+\frac{R_2^5}{r_2^3}\right) + O\left(\frac{1}{D^5}\right).\end{aligned} \tag{2.2}$$

The expressions for the potentials are valid, respectively, in the vicinity of bubbles 1 and 2.

3. Equations of motion for two pulsating and translating spherical gas bubbles

3.1. *The Oguz–Prosperetti virial theorem*

The Oguz–Prosperetti virial theorem is a tool that allows the two-bubble problem to be projected onto a system of ordinary differential equations for R_1, R_2, U_1 and U_2. In particular, we use the following refined version of the theorem.

THEOREM 1. *Consider a smooth, closed, time-dependent surface S immersed in an inviscid potential flow with velocity potential Φ. Let $\boldsymbol{u}=\nabla\Phi$ represent the velocity field of the flow and let $\boldsymbol{n}$ be the unit normal to S. Suppose $f: S\to\mathbb{R}$ is any differentiable function that can be extended to a small tubular neighbourhood of S. Then*

$$\frac{\mathrm{d}}{\mathrm{d}t}\int_{S(t)}\Phi f\,\mathrm{d}S = \int_{S(t)}\Phi\left[\frac{\mathrm{D}f}{\mathrm{D}t} - f\boldsymbol{n}\cdot(\nabla\boldsymbol{u})\cdot\boldsymbol{n}\right]\mathrm{d}S + \frac{1}{2}\int_{S(t)}(\boldsymbol{u}\cdot\boldsymbol{u})f\,\mathrm{d}S - \int_{S(t)}p'f\,\mathrm{d}S \tag{3.1}$$

where $p'=(p_\mathrm{L}-p_\infty(t))/\rho$, and p_L, $p_\infty(t)$ denote liquid pressures just outside S, and in the far field, respectively.

This result, which follows from equation (2.7) in Oguz & Prosperetti (1990), will be a key ingredient in the development of a two-bubble model. Roughly speaking, the theorem is obtained by combining the surface Reynolds transport theorem with Bernoulli's equation. A concise derivation is given in Appendix B. When applying (3.1) it should be noted that the operator $\mathrm{D}/\mathrm{D}t = \partial/\partial t + \boldsymbol{u}\cdot\nabla$ represents the material derivative with respect to the fluid velocity just outside the closed surface.

3.2. *Radial pulsations*

In the refined Oguz–Prosperetti virial theorem (3.1) let S denote the surface of a bubble. If we choose the function f to be given by $f = 1$, the theorem becomes

$$\frac{\mathrm{d}}{\mathrm{d}t}\int_S \Phi\,\mathrm{d}S = -\int_S \Phi[\boldsymbol{n}\cdot(\nabla\boldsymbol{u})\cdot\boldsymbol{n}]\,\mathrm{d}S + \frac{1}{2}\int_S \boldsymbol{u}\cdot\boldsymbol{u}\,\mathrm{d}S - \int_S p'\,\mathrm{d}S. \tag{3.2}$$

Substituting the two-bubble potential (2.1) and evaluating the surface integrals, we find up to order D^{-4}

$$R_1\ddot{R}_1 + \tfrac{3}{2}\dot{R}_1^2 = p_1' + \frac{U_1^2}{4} - \frac{2R_2\dot{R}_2^2 + R_2^2\ddot{R}_2}{D} + \frac{R_2^2\dot{R}_2(3U_1 + 3U_2 + 2\dot{D}) + R_2^3\dot{U}_2}{2D^2} - \frac{R_2^3U_2(3U_1 + 2\dot{D})}{2D^3} - \frac{4R_1^3R_2\dot{R}_2^2 + 6R_1^2R_2^2\dot{R}_1\dot{R}_2 - 3R_2^4\dot{R}_2^2 + 2R_1^3R_2^2\ddot{R}_2}{4D^4}, \tag{3.3}$$

where

$$p_1' = \frac{p_{\mathrm{L}}(R_1) - p_\infty(t)}{\rho} = \frac{1}{\rho}\left[\left(p_0^\infty + \frac{2\sigma}{R_{10}}\right)\left(\frac{R_{10}}{R_1}\right)^{3\kappa} - 4\mu\frac{\dot{R}_1}{R_1} - \frac{2\sigma}{R_1} - p_\infty(t)\right]. \tag{3.4}$$

Here, the far-field liquid pressure is $p_\infty(t) = p_0^\infty - p_A\cos(\Omega t)$. Also, we have added a damping term to the radial pulsations with $\mu = \mu_{\mathrm{vis}} + \mu_{\mathrm{th}} + \mu_{\mathrm{rad}}$ denoting an effective viscosity representing liquid viscosity, thermal damping and radiative damping. Note that we are using an effective damping coefficient, and hence assuming that acoustic streaming is not significant, see Doinikov (1997*a*).

In the same fashion, substituting Φ as given by (2.2) into (3.2) yields

$$R_2\ddot{R}_2 + \tfrac{3}{2}\dot{R}_2^2 = p_2' + \frac{U_2^2}{4} - \frac{2R_1\dot{R}_1^2 + R_1^2\ddot{R}_1}{D} - \frac{R_1^2\dot{R}_1(3U_1 + 3U_2 - 2\dot{D}) + R_1^3\dot{U}_1}{2D^2} + \frac{R_1^3U_1(3U_2 + 2\dot{D})}{2D^3} - \frac{4R_2^3R_1\dot{R}_1^2 + 6R_2^2R_1^2\dot{R}_2\dot{R}_1 - 3R_1^4\dot{R}_1^2 + 2R_2^3R_1^2\ddot{R}_1}{4D^4}, \tag{3.5}$$

where

$$p_2' = \frac{p_{\mathrm{L}}(R_2) - p_\infty(t)}{\rho} = \frac{1}{\rho}\left[\left(p_0^\infty + \frac{2\sigma}{R_{20}}\right)\left(\frac{R_{20}}{R_2}\right)^{3\kappa} - 4\mu\frac{\dot{R}_2}{R_2} - \frac{2\sigma}{R_2} - p_\infty(t)\right]. \tag{3.6}$$

(See Appendix C for an alternative derivation that does not depend on the Oguz–Prosperetti theorem.)

3.3. *Bubble translation*

To obtain equations governing translational motion, we choose $f = P_1(\cos\theta)$ in the refined Oguz–Prosperetti virial theorem (3.1):

$$\frac{\mathrm{d}}{\mathrm{d}t}\int_S \Phi P_1(\cos\theta)\,\mathrm{d}S = \int_S \Phi \frac{\mathrm{D}}{\mathrm{D}t} P_1(\cos\theta)\,\mathrm{d}S - \int_S \Phi[\boldsymbol{n}\cdot(\nabla u)\cdot\boldsymbol{n}]P_1(\cos\theta)\,\mathrm{d}S + \frac{1}{2}\int_S (\boldsymbol{u}\cdot\boldsymbol{u})P_1(\cos\theta)\,\mathrm{d}S - \int_S p' P_1(\cos\theta)\,\mathrm{d}S.$$

The material derivative $\mathrm{D}/\mathrm{D}t$ should be evaluated in fixed laboratory frame coordinates denoted by $\vec{x}$. The flow quantities are given in a frame moving with the bubble centre, whose local coordinates are denoted by $\vec{r}$. Hence, we will need the transformations

$$\left(\frac{\partial}{\partial t}\right)_{\vec{r}} = \left(\frac{\partial}{\partial t}\right)_{\vec{x}} + \boldsymbol{U}\cdot\nabla_{\vec{x}}, \qquad \nabla_{\vec{r}} = \nabla_{\vec{x}}.$$

For bubble 1, we substitute the two-bubble potential (2.1) and evaluate the surface integrals, finding up to order D^{-4}

$$\frac{\mathrm{d}}{\mathrm{d}t}\left[\frac{R_1^3U_1}{3} + \frac{R_1^3R_2^2\dot{R}_2}{D^2} - \frac{R_1^3R_2^3U_2}{D^3}\right] = \frac{2R_1^2\dot{R}_1R_2^2\dot{R}_2}{D^2} + \frac{2R_1^3R_2^2\dot{R}_2U_1 - 2R_2^3R_1^2\dot{R}_1U_2}{D^3} - \frac{3R_1^3R_2^3U_1U_2}{D^4}, \quad (3.7)$$

where terms of order D^{-5} and higher are omitted. Similarly, for bubble 2 we insert the velocity potential given by (2.2) and evaluate the integrals to find

$$\frac{\mathrm{d}}{\mathrm{d}t}\left[\frac{R_2^3U_2}{3} - \frac{R_2^3R_1^2\dot{R}_1}{D^2} + \frac{R_2^3R_1^3U_1}{D^3}\right] = -\frac{2R_2^2\dot{R}_2R_1^2\dot{R}_1}{D^2} + \frac{2R_2^3R_1^2\dot{R}_1U_2 + 2R_1^3R_2^2\dot{R}_2U_1}{D^3} + \frac{3R_1^3R_2^3U_1U_2}{D^4}. \quad (3.8)$$

An equivalent but more physically meaningful version of the translation equations is obtained by rewriting them in the form

$$\frac{\mathrm{d}}{\mathrm{d}t}\left[M_1\left(U_1 + \frac{3R_2^2\dot{R}_2}{D^2} - \frac{3R_2^3U_2}{D^3}\right)\right] = 2\pi\rho R_1^2R_2^2\left[\frac{2\dot{R}_1\dot{R}_2}{D^2} + \frac{2R_1\dot{R}_2U_1 - 2R_2\dot{R}_1U_2}{D^3} - \frac{3R_1R_2U_1U_2}{D^4}\right] + F_1^D, \quad (3.9)$$

$$\frac{\mathrm{d}}{\mathrm{d}t}\left[M_2\left(U_2 - \frac{3R_1^2\dot{R}_1}{D^2} + \frac{3R_1^3U_1}{D^3}\right)\right] = 2\pi\rho R_2^2R_1^2\left[-\frac{2\dot{R}_2\dot{R}_1}{D^2} + \frac{2R_2\dot{R}_1U_2 + 2R_1\dot{R}_2U_1}{D^3} + \frac{3R_2R_1U_1U_2}{D^4}\right] + F_2^D, \quad (3.10)$$

where

$$M_i = \tfrac{2}{3}\pi R_i^3\rho, \quad i = 1, 2, \quad (3.11)$$

is the apparent mass of each bubble, and a drag term has been added, given by

$$F_i^D = -12\pi\mu_{\mathrm{vis}}R_iU_i, \quad i = 1, 2,$$

which is the Levich drag (Magnaudet & Eames 2000) on a translating bubble.

The distance between the bubble centres is governed by the kinematic relation

$$\dot{D} = U_2 - U_1. \tag{3.12}$$

Equations (3.3), (3.5), (3.7), (3.8) and (3.12) fully determine the dynamics of the bubble pairs we study. They differ somewhat from the corresponding set of equations in Oguz & Prosperetti (1990), who used a low-order two-bubble potential as an illustration of how to apply their virial theorem.

4. An enhanced Bjerknes model in the weak forcing limit

In this section, we derive an enhanced Bjerknes model for two interacting gas bubbles in the presence of a weak acoustic field. The model incorporates the mutual coupling of the bubble radii and is self-consistent up to fourth order of accuracy in inverse powers of the separation distance. We begin in § 4.1 by showing how the equations of motion simplify in the presence of weak forcing. These simplified equations are then further reduced using the method of averaging in two main steps. For the first step, in § 4.2, we focus on fixed D and carry out a linear analysis on the coupled radial equations. Specifically, we allow both the amplitudes and the phases of the linear radial oscillations to depend upon the fixed separation distance, D. In the second step, § 4.3, D is again time dependent and we employ the results of the linear analysis to average each term in the translation equations over one acoustic driving cycle. These averaged translation equations constitute the enhanced Bjerknes model, which we analyse in § 5.

4.1. *The weak forcing model*

Up to this point, we have derived, to high order, equations of motion governing bubble radii (3.3), (3.5) and translation speeds (3.7), (3.8) or (including drag) (3.9), (3.10). For weak acoustic forcing (i.e. $p_A \ll p_0^\infty$), examination of the translation equations suggests that typical translation speeds are themselves of $O(1/D^2)$. Thus it is reasonable to conclude in this case that the terms in the radial equations (3.3) and (3.5) involving U_1 and U_2 are typically of $O(1/D^4)$ or higher, and hence they are relatively unimportant. This is a substantial simplification of the radial equations and points out that, after the $O(1/D)$ term, the next corrections are typically $O(1/D^4)$. By the same reasoning, in the translation equations (3.7), (3.8), the terms after those of order D^{-2} are found to be of order D^{-5}. This yields the following weak forcing model:

$$R_1\ddot{R}_1 + \tfrac{3}{2}\dot{R}_1^2 = p_1' - \frac{2R_2\dot{R}_2^2 + R_2^2\ddot{R}_2}{D}, \tag{4.1}$$

$$R_2\ddot{R}_2 + \tfrac{3}{2}\dot{R}_2^2 = p_2' - \frac{2R_1\dot{R}_1^2 + R_1^2\ddot{R}_1}{D}, \tag{4.2}$$

$$\frac{\mathrm{d}}{\mathrm{d}t}\left[M_1\left(U_1 + \frac{3R_2^2\dot{R}_2}{D^2}\right)\right] = 4\pi\rho\frac{R_1^2R_2^2\dot{R}_1\dot{R}_2}{D^2}, \tag{4.3}$$

$$\frac{\mathrm{d}}{\mathrm{d}t}\left[M_2\left(U_2 - \frac{3R_1^2\dot{R}_1}{D^2}\right)\right] = -4\pi\rho\frac{R_2^2R_1^2\dot{R}_2\dot{R}_1}{D^2}, \tag{4.4}$$

with M_i given by (3.11), p_i' given by (3.4) and (3.6), and with equation (3.12) determining the evolution of the centre-to-centre distance between the bubbles.

4.2. *Linear analysis of two coupled Rayleigh–Plesset equations*

When the separation distance between the bubbles is large compared to the bubble radii, equations (4.1) and (4.2) are a pair of weakly coupled Rayleigh–Plesset equations. Moreover, since the radial oscillations occur on a much faster time scale than changes in the separation distance, we may for the time being proceed as if $1/D$ were a small, constant coupling parameter. Hence, substituting $R_j = R_{j0}[1 + x_j(t)]$, $j = 1, 2$, into the weakly coupled Rayleigh–Plesset equations (4.1), (4.2) and linearizing, we find

$$\ddot{x}_1 + \zeta_1 \dot{x}_1 + \omega_{10}^2 x_1 + \epsilon_1 \ddot{x}_2 = P_1 \cos(\Omega t), \tag{4.5}$$

$$\ddot{x}_2 + \zeta_2 \dot{x}_2 + \omega_{20}^2 x_2 + \epsilon_2 \ddot{x}_1 = P_2 \cos(\Omega t), \tag{4.6}$$

where ζ_j, ω_{j0}^2 and P_j are given by (1.2) and

$$\epsilon_1 = \frac{R_{20}^3}{R_{10}^2 D}, \qquad \epsilon_2 = \frac{R_{10}^3}{R_{20}^2 D}. \tag{4.7}$$

Since $P_j \cos(\Omega t) = \mathrm{Re}[P_j \mathrm{e}^{\mathrm{i}\Omega t}]$, we let $x_j(t) = \delta_j \cos(\Omega t + \psi_j) = \mathrm{Re}[X_j \mathrm{e}^{\mathrm{i}\Omega t}]$, $j = 1, 2$, and the linearized system becomes

$$\begin{bmatrix} \omega_{10}^2 - \Omega^2 + \mathrm{i}\Omega\zeta_1 & -\epsilon_1\Omega^2 \\ -\epsilon_2\Omega^2 & \omega_{20}^2 - \Omega^2 + \mathrm{i}\Omega\zeta_2 \end{bmatrix} \begin{bmatrix} X_1 \\ X_2 \end{bmatrix} = \begin{bmatrix} P_1 \\ P_2 \end{bmatrix}.$$

Solving for X_1 and X_2 we get

$$X_1 = \frac{(\omega_{20}^2 - \Omega^2 + \mathrm{i}\Omega\zeta_2)P_1 + \epsilon_1\Omega^2 P_2}{(\omega_{10}^2 - \Omega^2 + \mathrm{i}\Omega\zeta_1)(\omega_{20}^2 - \Omega^2 + \mathrm{i}\Omega\zeta_2) - \epsilon_1\epsilon_2\Omega^4},$$

and

$$X_2 = \frac{(\omega_{10}^2 - \Omega^2 + \mathrm{i}\Omega\zeta_1)P_2 + \epsilon_2\Omega^2 P_1}{(\omega_{10}^2 - \Omega^2 + \mathrm{i}\Omega\zeta_1)(\omega_{20}^2 - \Omega^2 + \mathrm{i}\Omega\zeta_2) - \epsilon_1\epsilon_2\Omega^4}.$$

We can now compute

$$\delta_1 = \|X_1\| = \delta_1^0 \left(1 + \frac{\delta_1^1}{D} + O\left(\frac{1}{D^2}\right)\right),$$

$$\delta_2 = \|X_2\| = \delta_2^0 \left(1 + \frac{\delta_2^1}{D} + O\left(\frac{1}{D^2}\right)\right),$$

where $\|\cdot\|$ denotes the modulus and

$$\delta_1^0 = \frac{P_1}{\sqrt{(\omega_{10}^2 - \Omega^2)^2 + \Omega^2\zeta_1^2}}, \qquad \delta_1^1 = \frac{R_{20}^3 P_2 \Omega^2(\omega_{20}^2 - \Omega^2)}{R_{10}^2 P_1[(\omega_{20}^2 - \Omega^2)^2 + \Omega^2\zeta_2^2]},$$

$$\delta_2^0 = \frac{P_2}{\sqrt{(\omega_{20}^2 - \Omega^2)^2 + \Omega^2\zeta_2^2}}, \qquad \delta_2^1 = \frac{R_{10}^3 P_1 \Omega^2(\omega_{10}^2 - \Omega^2)}{R_{20}^2 P_2[(\omega_{10}^2 - \Omega^2)^2 + \Omega^2\zeta_1^2]}.$$

The phases ψ_1 and ψ_2 can be obtained via $\psi_j = \arg(X_j)$, $j = 1, 2$, and are also functions of D. Hence, for $\delta_j \ll 1$, the long-time solutions of the linearized, weakly coupled Rayleigh–Plesset equations are

$$R_j(t) \approx R_{j0}\left[1 + \delta_j^0\left(1 + \frac{\delta_j^1}{D}\right)\cos(\Omega t + \psi_j(D))\right], \quad j = 1, 2. \tag{4.8}$$

The importance of including the $1/D$ coupling term in the linear analysis is

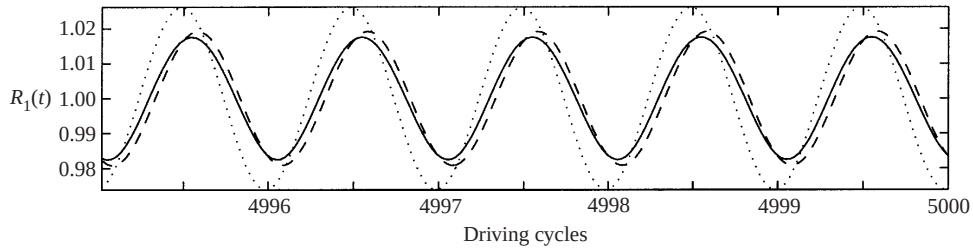

FIGURE 2. The solid curve is the radius of bubble 1 obtained from simulating the nonlinear equations (4.1)–(4.2) with D fixed at $D = 25R_{10}$. The dashed line is the radius calculated from the linearized, coupled Rayleigh–Plesset equations (4.5)–(4.6). The dotted curve is the radius used in classical Bjerknes theory, which is based on an uncoupled Rayleigh–Plesset equation. The $R(t)$ axis is scaled by R_{10}.

demonstrated in figure 2. Two bubbles of equilibrium radii $R_{10} = 120\,\mu\text{m}$ ($\omega_{10}/2\pi = 27.3\,\text{kHz}$) and $R_{20} = 102\,\mu\text{m}$ ($\omega_{20}/2\pi = 32.2\,\text{kHz}$) are forced at an acoustic pressure of $p_A = 5\,\text{kPa}$ and a frequency of $\Omega/2\pi = 32.8\,\text{kHz}$. The effective damping of the radial pulsations is taken to be $\mu = 20 \times \mu_{\text{vis}} = 20 \times 0.001\,\text{kg}\,\text{m}^{-1}\,\text{s}^{-1}$. The solid curve in figure 2 is the radius of bubble 1 obtained from numerically simulating the nonlinear equations (4.1), (4.2) with D fixed at $D = 25R_{10}$. The dotted curve is the linear solution of the uncoupled Rayleigh–Plesset equation for bubble 1 (i.e. it has constant phase and amplitude). Neither the phase nor the amplitude of the dotted curve agree well with the solid curve. In contrast, the dashed curve, which is the solution of the linearized, coupled Rayleigh–Plesset equations (4.5)–(4.6), agrees well with the (weakly) nonlinear solution.

4.3. *Averaging analysis of bubble translation*

In the weak forcing model, the translation variables $U_1(t)$, $U_2(t)$ and $D(t)$ evolve on a much slower time scale than do the bubble radii $R_1(t)$ and $R_2(t)$. It is thus reasonable that the long-term behaviour, $\bar{U}_1(t), \bar{U}_2(t), \bar{D}(t)$, of the slow translation variables can be represented well by time-averaging the radial coefficients in the translation equations (4.3)–(4.4). Substituting the explicit small-amplitude pulsation solutions (4.8) into the translation equations and integrating the radial coefficients over one forcing cycle ($T = 2\pi/\Omega$), we find

$$\frac{\mathrm{d}}{\mathrm{d}t}\left[M_{10}\bar{U}_1 + \frac{\gamma}{\bar{D}^2}\right] = \frac{\beta}{\bar{D}^2}, \qquad \frac{\mathrm{d}}{\mathrm{d}t}\left[M_{20}\bar{U}_2 + \frac{\gamma}{\bar{D}^2}\right] = -\frac{\beta}{\bar{D}^2}, \tag{4.9}$$

where for $j = 1, 2$ we have $M_{j0} = (2/3)\pi R_{j0}^3\rho + O(\delta_j^2)$. The averaged parameters β and γ are given in Appendix D, but since the parameter β is central to the subsequent theory of this section, we state its expression here for both emphasis and convenience:

$$\beta = 2\pi\rho\Omega^2 R_{10}^3 R_{20}^3\,\delta_1\delta_2\cos(\psi_1 - \psi_2) + O(\delta_1^3,\,\delta_2^3) \approx \beta^0 + \frac{\beta^1}{\bar{D}}, \tag{4.10}$$

where

$$\beta^0 = \frac{2\pi\rho\Omega^2 R_{10}^3 R_{20}^3 P_1 P_2 (W_1 W_2 + \Omega^2\zeta_1\zeta_2)}{(W_1^2 + \Omega^2\zeta_1^2)(W_2^2 + \Omega^2\zeta_2^2)},$$

$$\beta^1 = \frac{2\pi\rho\Omega^4 R_{10}^3 R_{20}^3 P_1 P_2 (R_{10} W_2 + R_{20} W_1)}{(W_1^2 + \Omega^2\zeta_1^2)(W_2^2 + \Omega^2\zeta_2^2)},$$

and $W_j = \omega_{j0}^2 - \Omega^2$. Substituting these expanded parameters into the averaged translation equations (4.9), expanding the time derivatives and keeping terms of up to order $\bar{D}^{-3}$ yields

$$M_{10}\dot{\bar{U}}_1 = \frac{\beta^0}{\bar{D}^2} + \frac{\beta^1}{\bar{D}^3}, \qquad M_{20}\dot{\bar{U}}_2 = -\frac{\beta^0}{\bar{D}^2} - \frac{\beta^1}{\bar{D}^3}.$$

Note that the term involving γ is of higher order, and hence it has been neglected. Solving for $\dot{\bar{U}}_1$ and $\dot{\bar{U}}_2$ we obtain the normal form of the averaged translation equations,

$$\dot{\bar{U}}_1 = \frac{\mathscr{B}_2}{\bar{D}^2} + \frac{\mathscr{F}_2}{\bar{D}^3}, \qquad \dot{\bar{U}}_2 = -\frac{\mathscr{B}_1}{\bar{D}^2} - \frac{\mathscr{F}_1}{\bar{D}^3}, \tag{4.11}$$

where for $j = 1, 2$,

$$\mathscr{B}_j = \frac{3R_{j0}^3\Omega^2 P_1 P_2(W_1 W_2 + \Omega^2\zeta_1\zeta_2)}{(W_1^2 + \Omega^2\zeta_1^2)(W_2^2 + \Omega^2\zeta_2^2)}, \tag{4.12}$$

$$\mathscr{F}_j = \frac{3R_{j0}^3\Omega^4 P_1 P_2(W_1 R_{20} + W_2 R_{10})}{(W_1^2 + \Omega^2\zeta_1^2)(W_2^2 + \Omega^2\zeta_2^2)}. \tag{4.13}$$

Equations (4.11)–(4.13), whose derivation is based on equation (4.8), extend the classical secondary Bjerknes theory. The essence of the enhanced Bjerknes theory of this section is that the phases and amplitudes of the coupled radial oscillations depend on $\bar{D}$, which leads to the presence of $1/\bar{D}^3$ terms in the translation equations whose coefficients are $\mathscr{F}_1$ and $\mathscr{F}_2$ as given above. By contrast, the standard Bjerknes analysis explicitly assumes that both the phases and amplitudes of the radial pulsations remain constant (i.e. do not depend upon relative distance $\bar{D}$). As a consequence, the translation equations obtained by standard Bjerknes analysis only contain $1/\bar{D}^2$ terms whose coefficients are $\mathscr{B}_1$ and $\mathscr{B}_2$ as given above.

5. Classification of the translational motions of two weakly forced bubbles

5.1. *Predictions of the enhanced Bjerknes theory*

The averaged translation equations (4.11) can be combined into a single second-order equation for the relative distance between the bubbles. Since $\ddot{\bar{D}} = \dot{\bar{U}}_2 - \dot{\bar{U}}_1$, we immediately obtain

$$\ddot{\bar{D}} = -\frac{\mathscr{B}}{\bar{D}^2} - \frac{\mathscr{F}}{\bar{D}^3}, \tag{5.1}$$

where

$$\mathscr{B} = \mathscr{B}_1 + \mathscr{B}_2 = \frac{3\Omega^2 P_1 P_2(R_{10}^3 + R_{20}^3)(W_1 W_2 + \Omega^2\zeta_1\zeta_2)}{(W_1^2 + \Omega^2\zeta_1^2)(W_2^2 + \Omega^2\zeta_2^2)},$$

$$\mathscr{F} = \mathscr{F}_1 + \mathscr{F}_2 = \frac{3\Omega^4 P_1 P_2(R_{10}^3 + R_{20}^3)(W_1 R_{20} + W_2 R_{10})}{(W_1^2 + \Omega^2\zeta_1^2)(W_2^2 + \Omega^2\zeta_2^2)}.$$

The Hamiltonian is $\bar{H} = \dot{\bar{D}}^2/2 + V(\bar{D})$, with $V(\bar{D}) = -\mathscr{B}/\bar{D} - \mathscr{F}/(2\bar{D}^2)$. Through a different argument, Barbat *et al.* (1999) arrived at a similar equation and used it to explain their experimental observations; however, in that work, the values of $\mathscr{B}$ and $\mathscr{F}$ are not given solely in terms of the material parameters of the problem. Here, we have derived explicit expressions for $\mathscr{B}$ and $\mathscr{F}$ from first principles and we state them in terms of the known liquid and acoustic properties (i.e. $p_A, \Omega, \omega_{j0}, R_{j0}, \rho, \mu$).

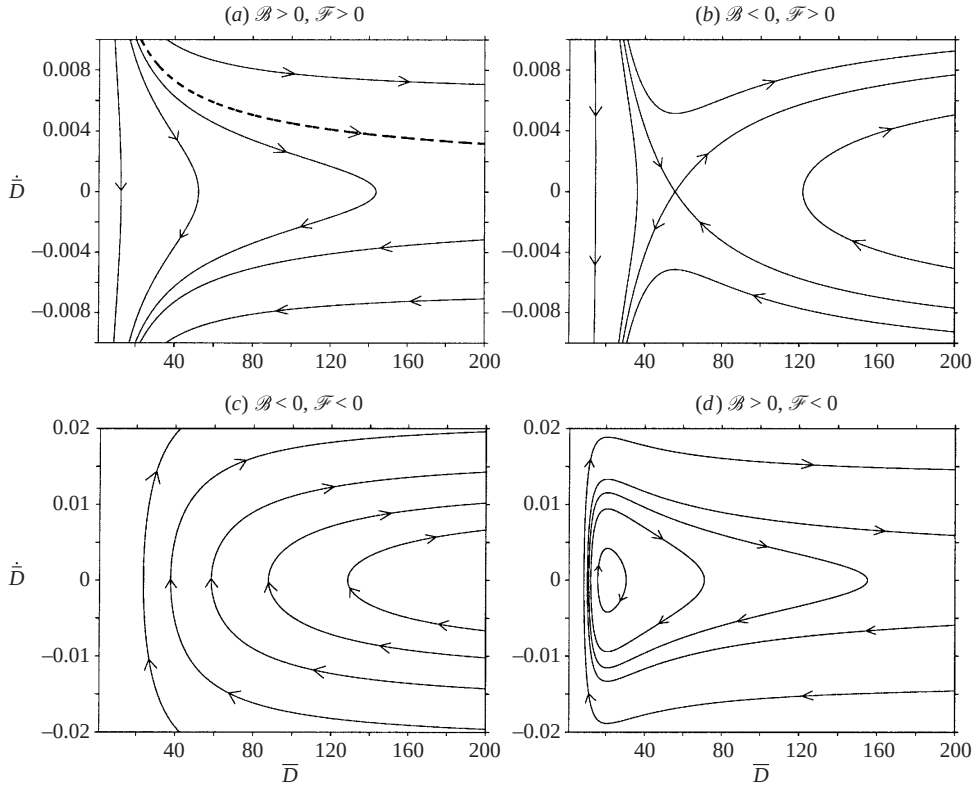

FIGURE 3. Phase planes of (5.1) ($\bar{D} > 0$) classifying possible trajectories of two interacting bubbles. Note: in all § 5 figures, the $\bar{D}$ axis is scaled by R_{10}.

Equation (5.1) has a single fixed point at $\bar{D} = -\mathscr{F}/\mathscr{B}$, and we are interested in physically relevant fixed points for which $\bar{D} > 0$. Moreover, the eigenvalues $\lambda_{1,2}$ of the equation linearized about this fixed point satisfy $\lambda^2 = \mathscr{B}^4/\mathscr{F}^3$, and thus we see that the equilibrium point at $(\bar{D}, \dot{\bar{D}}) = (-\mathscr{F}/\mathscr{B}, 0)$ is a saddle if $\mathscr{F} > 0$ and a centre if $\mathscr{F} < 0$. In figure 3, we examine the four distinct non-degenerate phase planes of (5.1) for positive $\bar{D}$.

The phase plane in figure 3(*a*) corresponds to the case in which the coefficients $\mathscr{B} > 0$ and $\mathscr{F} > 0$. There is a critical (dashed) trajectory that separates the phase half-plane. Trajectories above the critical trajectory will, as $t \to \infty$, have $\bar{D} \to \infty$, and trajectories below will have $\bar{D} \to 0$ (although some of those trajectories may at first have increasing $\bar{D}$). To obtain an expression for the critical trajectory we require $\dot{\bar{D}} \to 0$ as $\bar{D} \to \infty$. This is satisfied by $\bar{H} = 0$ or $\dot{\bar{D}} = \sqrt{2\mathscr{B}/\bar{D} + \mathscr{F}/\bar{D}^2}$ (escape velocity). So, in this case, two bubbles will eventually collide when $\bar{U}_2 - \bar{U}_1 < \sqrt{2\mathscr{B}/\bar{D} + \mathscr{F}/\bar{D}^2}$, and they will move apart forever when the inequality is reversed.

The phase plane in figure 3(*b*) corresponds to the case in which the coefficients $\mathscr{B} < 0$ and $\mathscr{F} > 0$. There is a saddle point on the $\bar{D}$-axis whose stable and unstable manifolds partition phase space into four regions. The energy of the saddle point is given by $\bar{H} = \mathscr{B}^2/(2\mathscr{F})$. The fate of a bubble pair is determined by which of the four regions its trajectory lies within. In this case we see that the possible patterns of motion are: attraction, repulsion, repulsion followed by attraction, and attraction followed by repulsion.

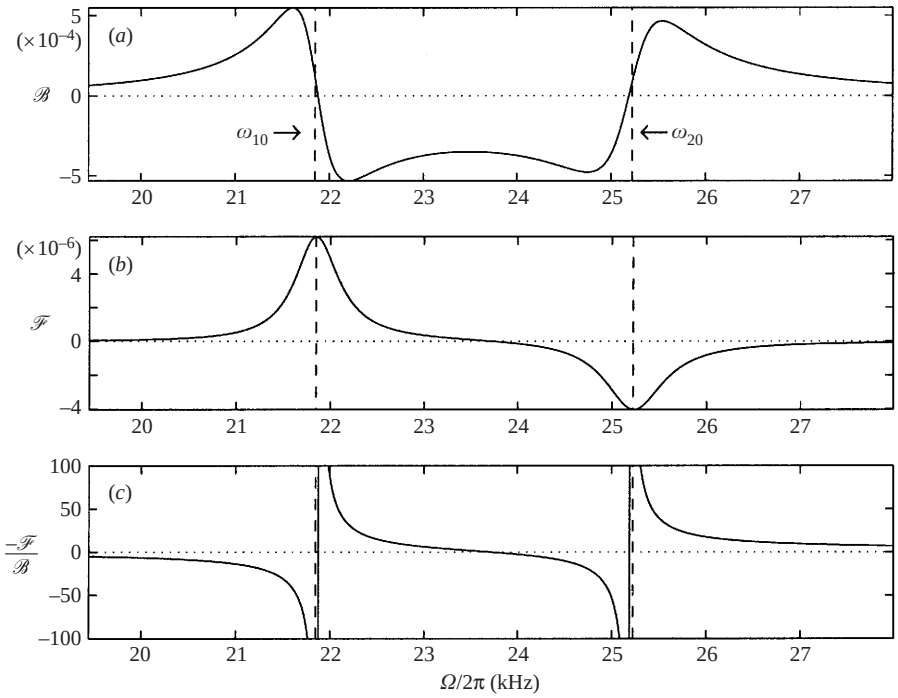

FIGURE 4. The coefficients $\mathscr{B}$ and $\mathscr{F}$ of (5.1), along with the fixed point at $\bar{D} = -\mathscr{F}/\mathscr{B}$, are shown for a wide range of forcing frequencies. The coefficient $\mathscr{B}$ has units of $\mathrm{m}^3\,\mathrm{s}^{-2}$, and $\mathscr{F}$ has units of $\mathrm{m}^4\,\mathrm{s}^{-2}$.

In figure 3(*c*), the coefficients of the planar system are $\mathscr{B} < 0$ and $\mathscr{F} < 0$. All trajectories in the phase plane eventually escape to infinity.

Lastly, in figure 3(*d*), the planar system coefficients are $\mathscr{B} > 0$ and $\mathscr{F} < 0$. The fixed point is a centre which is surrounded by a family of nested, closed trajectories. Thus, in this case, it is possible that the relative distance between two translating bubbles is periodic and stable. It should be noted that our analysis breaks down if the bubbles approach too closely; thus the detailed behaviour for cases in which $\bar{D}$ becomes small is not predicted by our model.

5.2. *Dependence of $\mathscr{B}$ and $\mathscr{F}$ on acoustic forcing frequency*

Next we examine the dependence of $\mathscr{B}$ and $\mathscr{F}$ on forcing frequency. The values of $\mathscr{B}$, $\mathscr{F}$ and the fixed point at $\bar{D} = -\mathscr{F}/\mathscr{B}$ are shown in figure 4 for a wide range of acoustic forcing frequencies Ω. The values of the parameters used to generate the figure are $R_{10} = 150\,\mu\mathrm{m}$ ($\omega_{10}/2\pi = 21.8\,\mathrm{kHz}$), $R_{20} = 130\,\mu\mathrm{m}$ ($\omega_{20}/2\pi = 25.2\,\mathrm{kHz}$), $p_A = 2\,\mathrm{kPa}$ and the total effective damping of the radial pulsations is $\mu = 20 \times \mu_{\mathrm{vis}} = 20 \times 0.001\,\mathrm{kg\,m^{-1}\,s^{-1}}$.

Figure 4(*a*) is a graph of the classical Bjerknes coefficient versus driving frequency. More specifically, classical Bjerknes theory yields $\ddot{\bar{D}} = -\mathscr{B}/\bar{D}^2$ and predicts that when two bubbles are both being driven either below or above their natural frequencies, they will attract each other. This is seen to be the case in figure 4(*a*), for in order to have $\mathscr{B} > 0$ either $\Omega < \omega_{10} < \omega_{20}$ or $\omega_{10} < \omega_{20} < \Omega$. Standard Bjerknes theory also predicts that when one bubble is being driven below its natural frequency and the other bubble is being driven above its, the bubbles will repel. This corresponds precisely to the domain on which $\mathscr{B} < 0$.

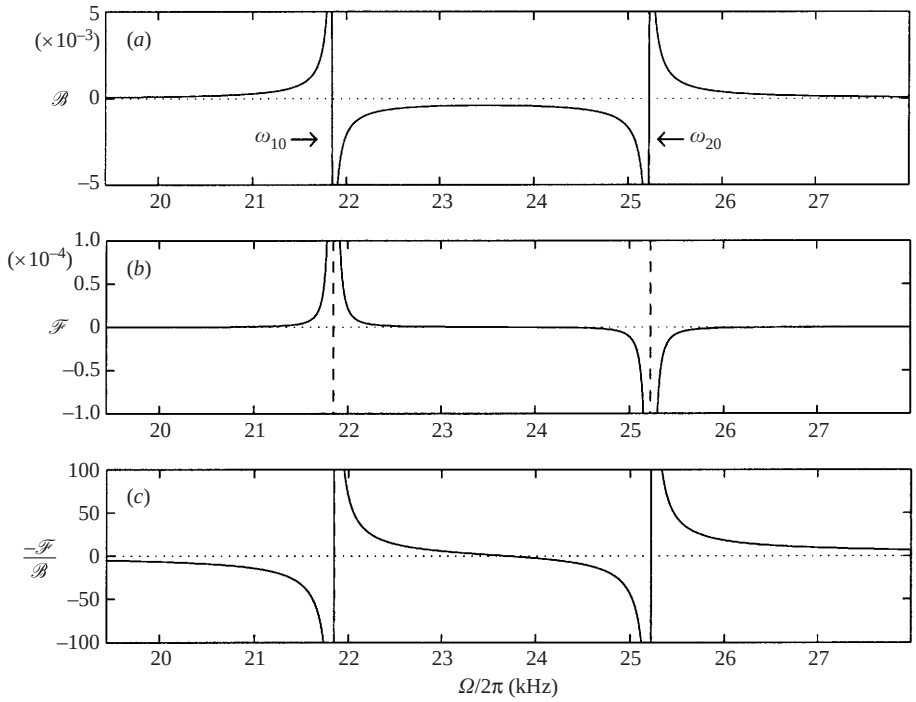

FIGURE 5. The effect of weak damping, $\mu = \mu_{\text{vis}} = 0.001\,\text{kg}\,\text{m}^{-1}\,\text{s}^{-1}$, on the coefficients $\mathscr{B}$, $\mathscr{F}$ and the fixed point $\bar{D} = -\mathscr{F}/\mathscr{B}$. The parameters are $R_{10} = 150\,\mu\text{m}$, $R_{20} = 130\,\mu\text{m}$ and $p_A = 2\,\text{kPa}$.

The coefficient $\mathscr{F}$ arising from enhanced Bjerknes theory is graphed versus $\Omega/2\pi$ in figure 4(*b*). We emphasize that the existence of the stable and unstable equilibrium points for (5.1) is only possible because of the presence of the $\mathscr{F}/\bar{D}^3$ term.

The fixed point at $\bar{D} = -\mathscr{F}/\mathscr{B}$ is graphed versus $\Omega/2\pi$ in figure 4(*c*) (of course, only positive values of $\bar{D}$ are physical). The equilibria that occur slightly to the right of the resonance frequency ω_{10} are unstable, whereas those slightly to the right of the resonance at ω_{20} are stable. We also observe that as the forcing frequency approaches either natural frequency from above, the magnitudes of the equilibria become larger. It is thus seen that stable bound pair oscillations, corresponding to figure 3(*d*), occur when the forcing frequency is slightly larger than the larger of the two Minnaert frequencies of the bubbles.

The next set of plots in figure 5 illustrate how the coefficients $\mathscr{B}, \mathscr{F}$ and the fixed point $\bar{D} = -\mathscr{F}/\mathscr{B}$ behave in the limit of weak damping of the radial oscillations (i.e. $\mu = \mu_{\text{vis}}$). We observe that while the specific values of $\mathscr{B}$ and $\mathscr{F}$ change over the same range of frequencies as compared to the larger damped simulations shown in figure 4, the four combinations of signs of $\mathscr{B}$ and $\mathscr{F}$ (i.e. $++$, $+-$, $-+$, $--$) still occur for a specific partition of the forcing frequency domain. Hence, all of the qualitative motions for two bubbles that have been discussed in this section are all still possible for two weakly damped bubbles.

The results of figures 4 and 5 are based upon a pair of bubbles having unequal equilibrium radii $R_{10} = 150\,\mu\text{m}$ and $R_{20} = 130\,\mu\text{m}$. It turns out that, for two bubbles having the same equilibrium radius, only two phase planes are encountered over a wide range of forcing frequencies (figure 6). They are the phase planes having $\mathscr{B} > 0$, $\mathscr{F} > 0$ and $\mathscr{B} > 0$, $\mathscr{F} < 0$. When the bubbles are forced below their natural

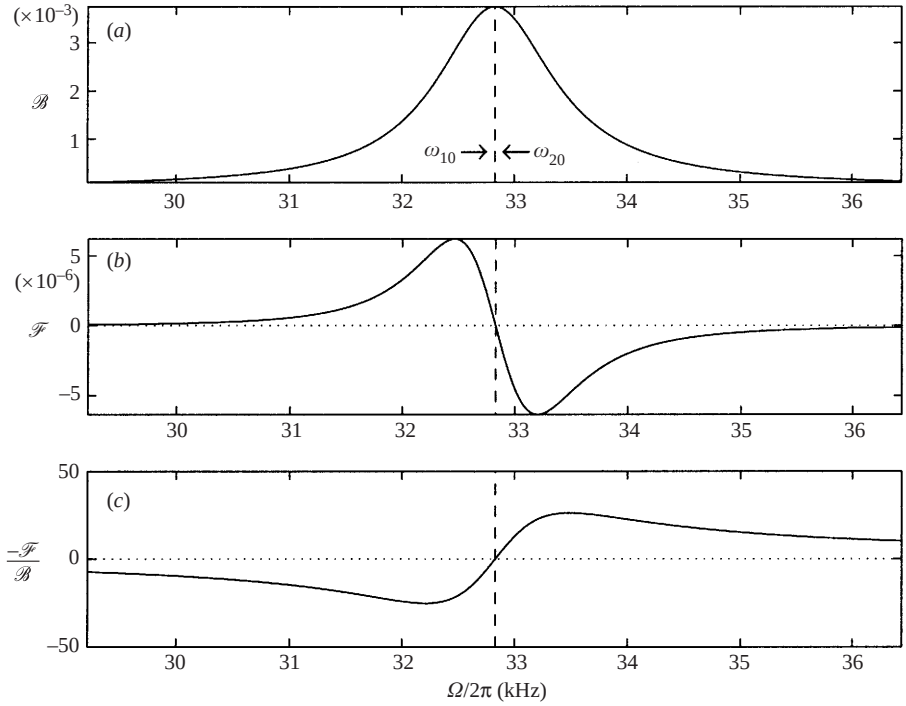

FIGURE 6. The coefficients $\mathscr{B}$, $\mathscr{F}$ and the fixed point $\bar{D} = -\mathscr{F}/\mathscr{B}$ when the equilibrium radii of the bubbles are equal, $R_{10} = R_{20} = 100\,\mu\text{m}$ ($\omega_{10}/2\pi = \omega_{20}/2\pi = 32.8\,\text{kHz}$). The other parameters are $p_A = 2\,\text{kPa}$ and $\mu = 20 \times 0.001\,\text{kg m}^{-1}\,\text{s}^{-1}$.

frequency, both $\mathscr{B}$ and $\mathscr{F}$ are positive, and hence, based upon the initial velocities of the bubbles, they can either attract, repel, or repel then attract. Alternatively, when the bubbles are forced at a frequency above their natural frequency, $\mathscr{B} > 0$ and $\mathscr{F} < 0$, and therefore the enhanced Bjerknes theory predicts oscillatory motion of the two bubbles around a stable separation distance (provided that $\bar{D}$ does not become too small for the theory to break down).

5.3. *Bifurcation diagram for summarizing patterns of translation*

The enhanced Bjerknes theory completely classifies (via figure 3) the fate of a pair of interacting bubbles through the signs of the parameters $\mathscr{B}$ and $\mathscr{F}$. For fixed equilibrium bubble radii, figures 4, 5 and 6 illustrate the dependence of $\mathscr{B}$ and $\mathscr{F}$ upon forcing frequency Ω. By contrast, in figure 7 we instead choose to fix the forcing frequency and illustrate the dependence of $\mathscr{B}$ and $\mathscr{F}$ upon equilibrium radii (R_{10}, R_{20}). We consider equilibrium bubble radii between 1 and 200 μm, whose radial oscillations are damped with $\mu = 20 \times \mu_{\text{vis}}$ and driven at a frequency of $\Omega/2\pi = 32.8\,\text{kHz}$. The solid curves partitioning the (R_{10}, R_{20})-plane in figure 7 are given implicitly by

$$\mathscr{B} = 0 \Rightarrow (\omega_{10}^2 - \Omega^2)(\omega_{20}^2 - \Omega^2) + \Omega^2\zeta_1\zeta_2 = 0,$$
$$\mathscr{F} = 0 \Rightarrow (\omega_{10}^2 - \Omega^2)R_{20} + (\omega_{20}^2 - \Omega^2)R_{10} = 0,$$

where ω_{j0}^2, ζ_j are given by (1.2).

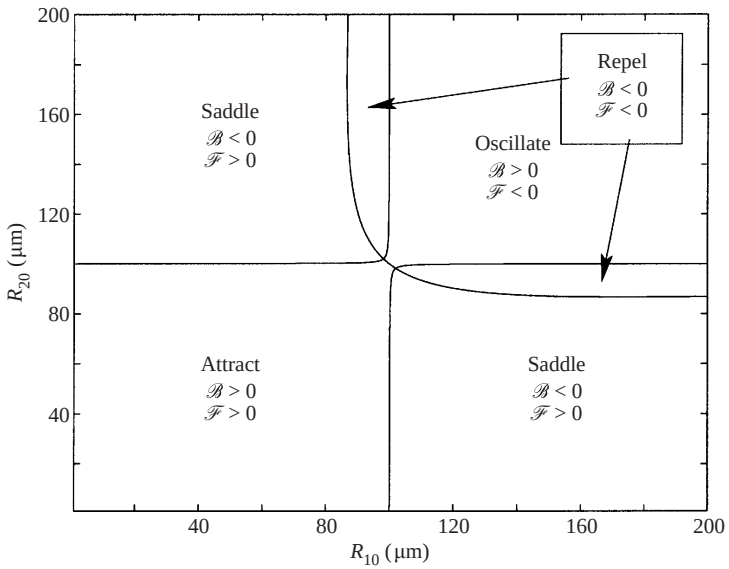

FIGURE 7. Relative signs of $\mathscr{B}$ and $\mathscr{F}$ for a wide range of equilibrium radii. The parameters are $\Omega/2\pi = 32.8\,\text{kHz}$ and $\mu = 20 \times \mu_{\text{vis}} = 20 \times 0.001\,\text{kg m}^{-1}\,\text{s}^{-1}$.

5.4. *Numerical simulations of the weak forcing model*

In this section we compare analytical predictions of enhanced Bjerknes theory to direct numerical simulations of the weak forcing model (4.1)–(4.4) and (3.12). More specifically, for selected bubble pairs corresponding to (R_{10}, R_{20}) points in figure 7, we compare the numerical time series of the weak forcing model to the outcome predicted by the bifurcation diagram.

The first bubble pair chosen for simulation yields perhaps the most interesting pattern of motion predicted by enhanced Bjerknes theory: the oscillation of two bubble centres about a stable equilibrium separation distance. Consider in figure 8 two unequal sized bubbles of equilibrium radii $R_{10} = 120\,\mu\text{m}$ ($\omega_{10}/2\pi = 27.3\,\text{kHz}$) and $R_{20} = 102\,\mu\text{m}$ ($\omega_{20}/2\pi = 32.2\,\text{kHz}$). The bubbles are assumed to be damped by an effective viscosity $\mu = 20 \times \mu_{\text{vis}}$ and forced at frequency $\Omega/2\pi = 32.8\,\text{kHz}$ and amplitude $p_A = 500\,\text{Pa}$. Enhanced Bjerknes theory predicts that $\mathscr{B} > 0$, $\mathscr{F} < 0$ (figure 7), and hence, the two bubble centres will undergo oscillatory motion around the stable separation distance $\bar{D}_{centre} = -\mathscr{F}/\mathscr{B} = 23R_{10}$. In figure 8, the numerical simulation of the unaveraged weak forcing equations (3.12)–(4.4) shows excellent agreement with the prediction of enhanced Bjerknes theory.

Next, we confirm the prediction that the oscillatory translational motion seen in the solid curves of figure 8 (and of figure 12 below) truly is a consequence of the coupled radial pulsations. For this purpose, in figure 9, we numerically simulate the weak forcing model with the modification that the Rayleigh–Plesset equations are decoupled. The parameters are exactly the same as those of figure 8, which gave rise to oscillations in $D(t)$. The figure shows that two bubbles that pulsate independently do not translate in an oscillatory manner.

Among the other predictions of enhanced Bjerknes theory is the possibility of an unstable equilibrium distance between two bubbles. Recall from § 4.3 the averaged equations $M_{10}\dot{\bar{U}}_1 = \beta/\bar{D}^2$ and $M_{20}\dot{\bar{U}}_2 = -\beta/\bar{D}^2$. Thus, we can interpret the sign of β as the direction of the mutual force between the bubbles, a positive sign indicating

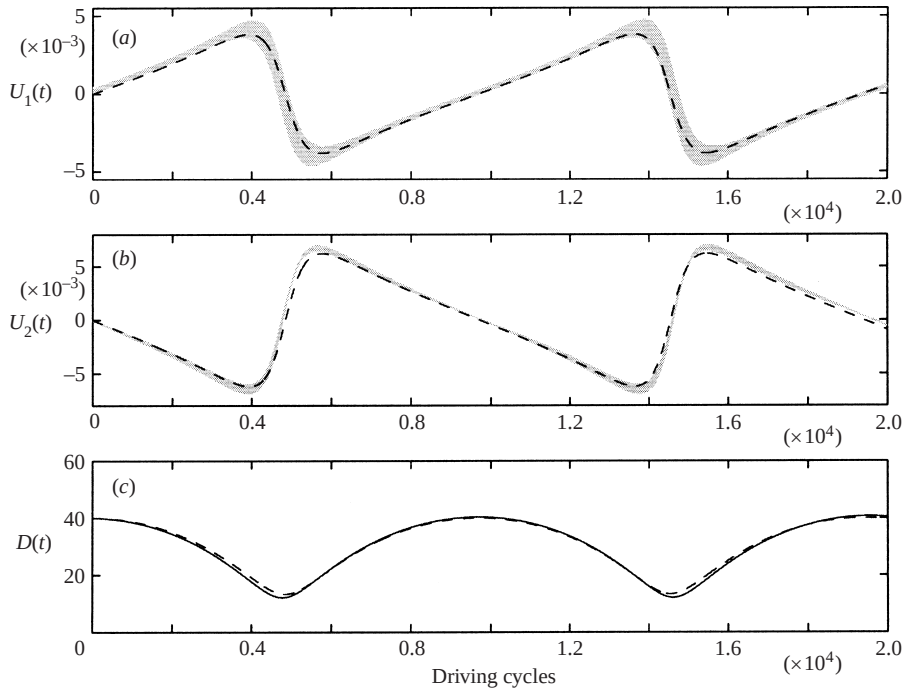

FIGURE 8. Comparison between the averaged (dashed) versus unaveraged (solid, greyish) weak forcing model: U_1, U_2 and D are plotted over 20 000 cycles of the acoustic forcing.

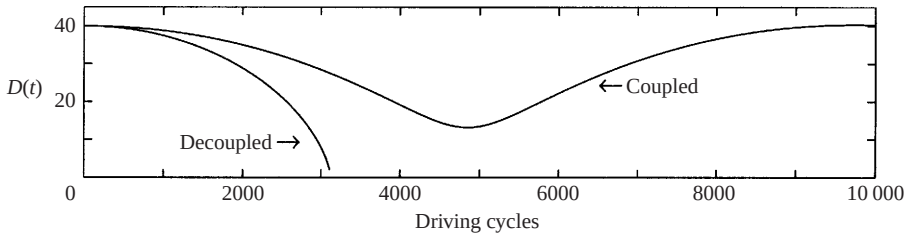

FIGURE 9. Numerical simulation of the weak forcing model with decoupled radial pulsations versus the weak forcing model with coupled pulsations.

attraction and a negative sign repulsion. Consider in figure 10 the graph of β versus centre-to-centre distance for a pair of bubbles of equilibrium radii $R_{10} = 101.5\,\mu\text{m}$ ($\omega_{10}/2\pi = 32.3\,\text{kHz}$) and $R_{20} = 80\,\mu\text{m}$ ($\omega_{20}/2\pi = 41.1\,\text{kHz}$). We see that for $\bar{D}$ smaller than $\bar{D}_{saddle} = -\mathscr{F}/\mathscr{B} = 37.7R_{10}$, the sign of β is positive and the bubbles attract each other. Similarly, for $\bar{D}$ larger than $\bar{D}_{saddle}$, the bubbles repel. Therefore, we expect an unstable equilibrium located at $\bar{D}_{saddle} = 37.7R_{10}$.

The numerical simulations shown in figure 11 confirm that the unaveraged weak forcing model also exhibits the behaviour associated with an unstable equilibrium, $\bar{D}_{saddle}$. For the bubble pair of figure 10, the enhanced Bjerknes theory predicts that $\mathscr{B} < 0$, $\mathscr{F} > 0$. Hence, the two bubbles will either attract or repel depending upon whether their initial separation is smaller or larger, respectively, than the saddle point $\bar{D}_{saddle} = -\mathscr{F}/\mathscr{B} = 37.7R_{10}$. In the top curve of figure 11, the initial separation is $D(0) > \bar{D}_{saddle}$, and the bubbles repel forever. In the bottom curve, the initial separation is $D(0) < \bar{D}_{saddle}$, and the bubbles attract.

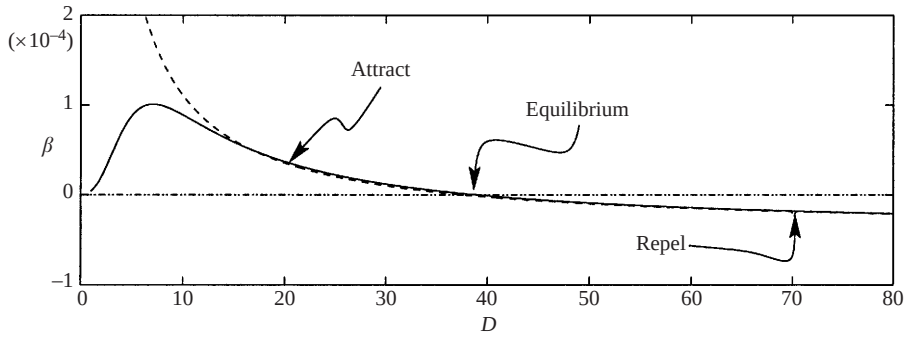

FIGURE 10. The direction of the mutual force between two bubbles as a function of centre-to-centre distance. The parameters are $R_{10} = 101.5\,\mu\text{m}$ ($\omega_{10}/2\pi = 32.3\,\text{kHz}$), $R_{20} = 80\,\mu\text{m}$ ($\omega_{20}/2\pi = 41.1\,\text{kHz}$), $\Omega/2\pi = 32.8\,\text{kHz}$, $p_A = 500\,\text{Pa}$ and $\mu = 20 \times 0.001\,\text{kg m}^{-1}\,\text{s}^{-1}$. The solid curve graphs equation (4.10) for β. The dashed curve is the expansion of β in powers of $1/\bar{D}$.

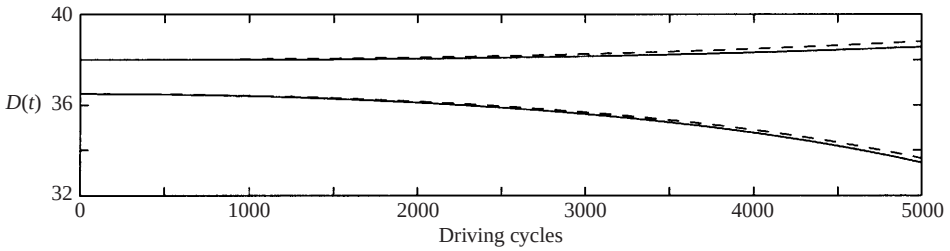

FIGURE 11. The solid curves represent two solutions for $D(t)$ with initial conditions on different sides of an unstable equilibrium separation at $\bar{D}_{saddle} = 37.7R_{10}$. The dashed curves are the predictions for $\bar{D}(t)$ based upon the averaged equations.

6. Nonlinear secondary Bjerknes force in the limit of moderate acoustic forcing

6.1. *The breakdown of weak forcing theory*

As the external forcing pressure increases, the size of the separation distance D needed for either the Bjerknes theory or the enhanced Bjerknes theory to be valid increases. We now quantify how the weak forcing assumption begins to break down when the forcing pressure is taken to be moderately large, even for bubbles that are relatively far apart.

Figure 12 demonstrates the gradually increasing disagreement between the averaged and unaveraged translation equations as forcing pressure increases. The same parameters as in figure 8 are used except the forcing pressure is increased to $p_A = 1000\,\text{Pa}$. The velocities are no longer asymptotically given by $U \sim 1/D^2$, and the oscillation amplitudes of the solutions to the unaveraged equations are slowly growing. Moreover, since the forcing is larger, the amplitudes of the radial oscillations (not shown in the figure) are larger as well. Recall that the amplitude of the radial oscillations is the small parameter employed in our averaging analysis. The averaging theorem then anticipates that our averaged solution (dashed curves) will break down sooner as the averaging parameter gets larger. This is clearly seen in figure 12 where the averaged solution breaks down near 10 000 forcing cycles, whereas for $p_A = 500\,\text{Pa}$ (figure 8) the averaged solution was accurate over 20 000 forcing cycles.

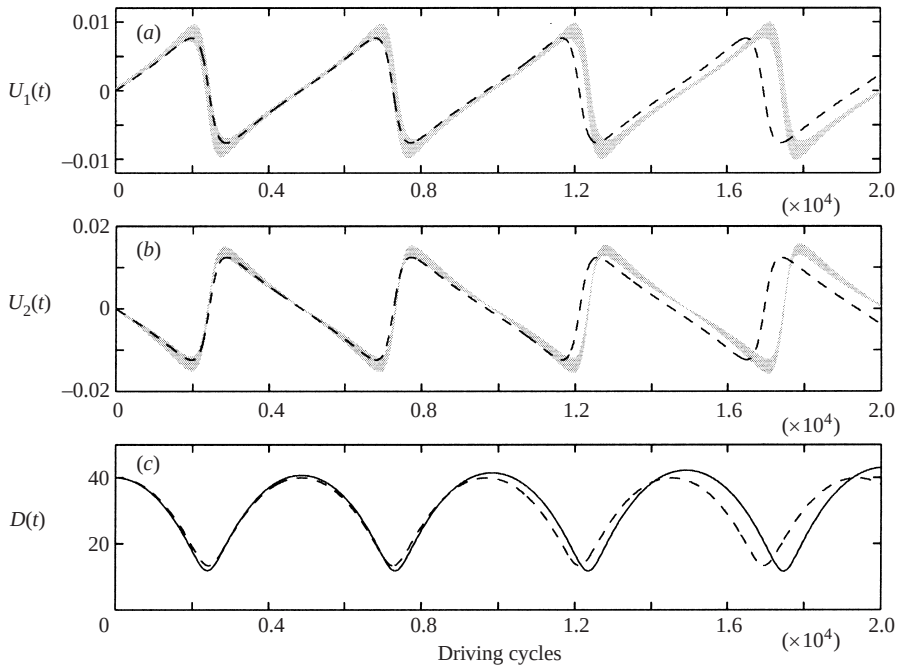

FIGURE 12. Comparison between the averaged (dashed) versus unaveraged (solid, greyish) weak forcing model as the weak forcing assumption becomes invalid.

6.2. *Coupling translation into the radial oscillations*

For a two-bubble model valid in the limit of moderate acoustic forcing, terms involving U_1 and U_2 in the radial equations of motion (3.3), (3.5) must be included. This provides direct coupling of translation to radial pulsations (as opposed to the indirect coupling coming through terms involving D). Hence, the following fully coupled model derived in § 3 will be examined in the rest of this section:

coupled Rayleigh–Plesset equations

$$R_1\ddot{R}_1 + \tfrac{3}{2}\dot{R}_1^2 = p_1' - \frac{2R_2\dot{R}_2^2 + R_2^2\ddot{R}_2}{D} + \frac{U_1^2}{4} + \frac{R_2^2\dot{R}_2(3U_1 + 3U_2 + 2\dot{D}) + R_2^3\dot{U}_2}{2D^2}, \quad (6.1)$$

$$R_2\ddot{R}_2 + \tfrac{3}{2}\dot{R}_2^2 = p_2' - \frac{2R_1\dot{R}_1^2 + R_1^2\ddot{R}_1}{D} + \frac{U_2^2}{4} - \frac{R_1^2\dot{R}_1(3U_1 + 3U_2 - 2\dot{D}) + R_1^3\dot{U}_1}{2D^2}; \quad (6.2)$$

translation equations

$$\frac{\mathrm{d}}{\mathrm{d}t}\left[\frac{R_1^3U_1}{3} + \frac{R_1^3R_2^2\dot{R}_2}{D^2}\right] = \frac{2R_1^2\dot{R}_1R_2^2\dot{R}_2}{D^2}, \quad (6.3)$$

$$\frac{\mathrm{d}}{\mathrm{d}t}\left[\frac{R_2^3U_2}{3} - \frac{R_2^3R_1^2\dot{R}_1}{D^2}\right] = -\frac{2R_2^2\dot{R}_2R_1^2\dot{R}_1}{D^2}. \quad (6.4)$$

We saw in figure 7 that the enhanced Bjerknes theory partitioned the R_{10}, R_{20} parameter space into disjoint regions which completely classified the possible long-term motions of weakly forced bubble pairs. Here, we numerically simulate the above

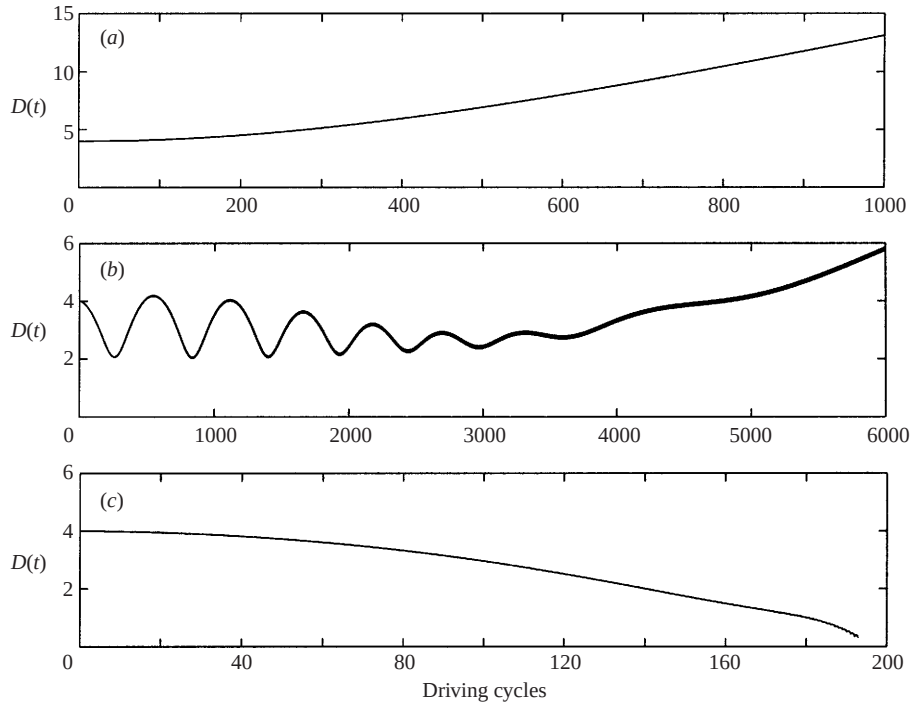

FIGURE 13. Three time-series are shown for the relative distance as the forcing pressure increases: $p_A = 10\,\text{kPa}$ (*a*), $p_A = 46\,\text{kPa}$ (*b*), $p_A = 50\,\text{kPa}$ (*c*). The equilibrium radii are $R_{10} = 105\,\mu\text{m}$ ($\omega_{10}/2\pi = 31.3\,\text{kHz}$), $R_{20} = 50\,\mu\text{m}$ ($\omega_{20}/2\pi = 66\,\text{kHz}$) and the forcing frequency is $\Omega/2\pi = 32.8\,\text{kHz}$. The D-axis is given in mm.

fully coupled model for the same forcing frequency, $\Omega/2\pi = 32.8\,\text{kHz}$, as in figure 7, but for higher forcing pressures.

We carry out three numerical simulations for a bubble pair having equilibrium radii $R_{10} = 105\,\mu\text{m}$ ($\omega_{10}/2\pi = 31.3\,\text{kHz}$) and $R_{20} = 50\,\mu\text{m}$ ($\omega_{20}/2\pi = 66\,\text{kHz}$), and effective damping $\mu = 20\times\mu_{\text{vis}}$. For weak acoustic forcing, this bubble pair lies near the leftmost boundary of the lower right quadrant of figure 7, and thus enhanced Bjerknes theory predicts an unstable equilibrium at $\bar{D}_{\text{saddle}} = 1.1\,\text{mm}$. For an initial separation distance $D(0) = 4\,\text{mm} > \bar{D}_{\text{saddle}}$, the bubbles will repel forever. This is seen in (*a*) of figure 13 where the bubbles are forced at a relatively low pressure of $p_A = 10\,\text{kPa}$. Increasing the forcing pressure to $p_A = 46\,\text{kPa}$ yields an interesting pattern of motion. In figure 13(*b*) we see that the bubble pair undergoes an initial period of oscillatory translational motion, followed by mutual repulsion. If the forcing pressure is further increased to $p_A = 50\,\text{kPa}$ (figure 13*c*), the bubbles attract and collide. Hence, moderate to strong acoustic forcing can reverse the long-term behaviour of two bubbles from that predicted by both classical and enhanced Bjerknes theory.

6.3. *Bifurcation diagrams and resonance zones*

In this section, we generate bifurcation diagrams that classify the *initial* motions of moderately forced bubbles. The numerical simulations of bubble pairs in this section are carried out with the moderate forcing model (6.1)–(6.4) and (3.12). It is first checked in figure 14(*a*) that the moderate forcing model, in the limit of weak forcing, $p_A = 5\,\text{kPa}$, can produce the same bifurcation diagram as does the weak forcing model (figure 7). For each point in the R_{10}, R_{20} parameter space, the moderate forcing model

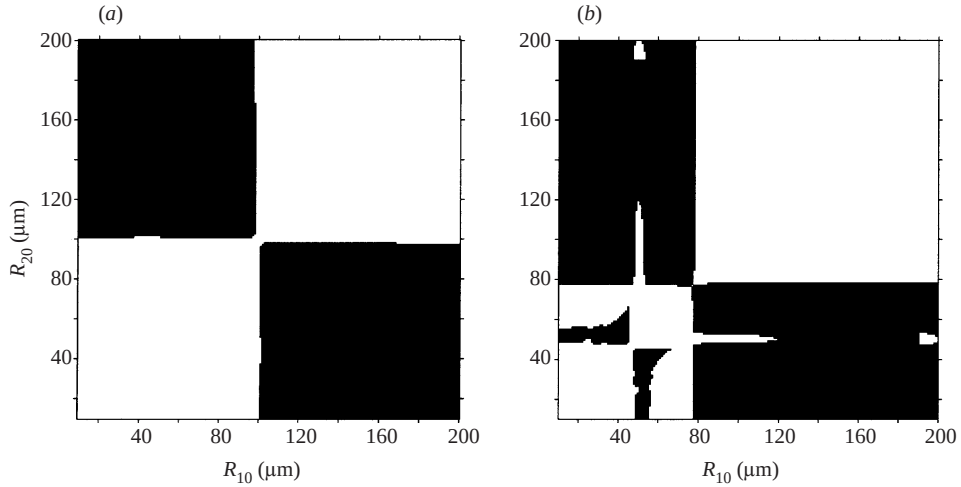

FIGURE 14. Bifurcation diagrams for bubble pairs being forced at $\Omega/2\pi = 32.8\,\text{kHz}$. In (*a*), the forcing is $p_A = 5\,\text{kPa}$ and in (*b*), $p_A = 50\,\text{kPa}$. The bubble pairs in the white regions initially attract each other, in the black regions they initially repel.

is integrated for a fixed time of 100 driving cycles. The driving frequency and the effective damping are chosen to be the same values as those used to generate figure 7, namely $\Omega/2\pi = 32.8\,\text{kHz}$ and $\mu = 20 \times \mu_{\text{vis}}$. Initially, the bubbles are resting at their equilibrium radii and have a separation distance of 4 mm. When the simulation for a particular bubble pair is finished, if the two bubbles are farther apart than initially, a black dot is assigned to the point in parameter space. If they become closer, the point is left white. Given the complexity of the moderate forcing model, we have only integrated each initial condition for some short time interval. Therefore, the bifurcation diagram only contains information about the *initial* attraction or repulsion of bubble pairs. Using the procedure just described, we next generate a bifurcation diagram for increased acoustic forcing, $p_A = 50\,\text{kPa}$. We see in figure 14(*b*), that under moderate acoustic forcing the R_{10}, R_{20} parameter space is still roughly divided into four regions.

The effects of the harmonic resonances of the radial pulsations are now clearly visible. In particular, these resonances cause a region in the lower left quadrant to turn black. This is evidence that bubble pairs that would attract according to the classical secondary Bjerknes theory, might repel due to nonlinear effects. To see that this is a harmonic resonance effect, note that the equilibrium radii of the bubbles in that region (roughly around 50 μm) are about half the size of the bubbles which resonate at the forcing frequency Ω. Since the resonant frequency of a bubble is inversely proportional to its radius, these 50 μm bubbles have a natural frequency which is almost twice the forcing frequency. Under moderate-amplitude forcing, they therefore exhibit a strong response due to a 2 : 1 resonance. It is also noteworthy that the dark regions are located above or below the main diagonal in figure 14 (right). This suggests that one of the bubbles is slightly larger than (roughly) 50 μm and the other slightly smaller. As such their natural frequencies actually lie on either side of 2Ω. The resulting repulsion (black region) is thus probably due to the fact that the bubbles have strong components with frequency 2Ω which are out of phase with respect to one another. The occurrence of a second harmonic resonance in the presence of moderate acoustic forcing has also been observed in Oguz & Prosperetti (1990).

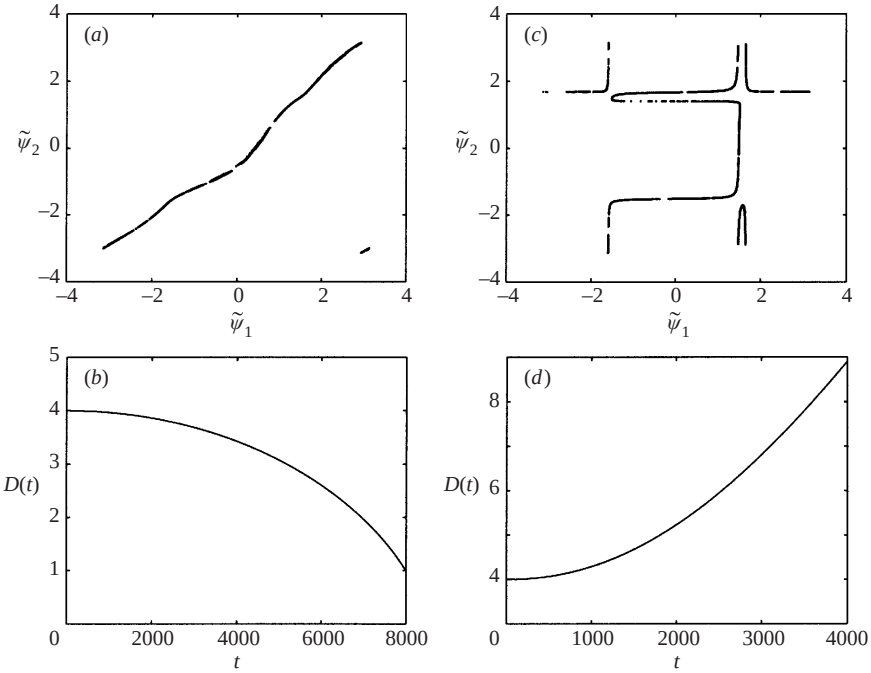

FIGURE 15. The effects of nonlinear phase shifting. In (a, b), where $p_A = 2\,\mathrm{kPa}$, the pulsation phases are coherent (a) and the bubbles attract each other (b). In (c, d), the forcing amplitude is larger, $p_A = 25\,\mathrm{kPa}$, and the anticoherence of the pulsation phases (c) leads to mutual repulsion of the bubbles (d). The relative distance D is given in mm.

The boundaries separating the various regions also become more intricate. Resonance tongues penetrate into the boundaries, so that parts of the regions that were previously black for lower forcing have become white, and vice versa. This is reminiscent of the behaviour observed in figure 13. Moreover, the deformations of the boundaries between the various regions are qualitatively similar to the boundaries seen in bifurcation diagrams presented by Mettin *et al.* (1997), albeit there the bubble centres are fixed. When bubble pairs are chosen which are well within the white or dark regions in the bifurcation diagram, their long-time dynamics generally follow the predictions based on the short-time simulations summarized in figure 14.

Lastly we illustrate, in figure 15, the effect of nonlinear phase shifting on the long-term fate of a bubble pair. Here, the nonlinear phases of bubbles 1 and 2 are defined through the relations

$$\tilde{\psi}_1 = \arctan\left(\frac{\dot{R}_1}{R_1 - R_{10}}\right), \qquad \tilde{\psi}_2 = \arctan\left(\frac{\dot{R}_2}{R_2 - R_{20}/R_{10}}\right).$$

In figure 15, two numerical simulations of the moderate forcing model are carried out with different forcing pressures for a bubble pair of equilibrium radii $R_{10} = 53\,\mu\mathrm{m}$ ($\omega_{10}/2\pi = 62.2\,\mathrm{kHz}$) and $R_{20} = 45\,\mu\mathrm{m}$ ($\omega_{20}/2\pi = 73.4\,\mathrm{kHz}$), and forcing frequency $\Omega/2\pi = 32.8\,\mathrm{kHz}$. The bubbles are initially at rest with a separation distance of 4 mm. For low-amplitude forcing, $p_A = 2\,\mathrm{kPa}$, in figure 15(a, b), we see that phase locking of the pulsations (a) leads to attraction of the bubbles (b). In figure 15(c, d), the forcing amplitude is larger, $p_A = 25\,\mathrm{kPa}$, and the phase anticoherence of the pulsations (c) leads to mutual repulsion of the bubbles (d).

7. Conclusions

Using ideas and techniques from dynamical systems theory, we have explored the problem of two spherical bubbles in a sound field that are coupled through their pulsations and translations. Employing a refined version of the Oguz–Prosperetti virial theorem, along with a two-bubble velocity potential containing interaction terms, we were able to derive the equations of motion for the radii and translation speeds of each bubble that are accurate up to and including the fourth order in the inverse separation distance. Analysis of these equations has led to the development of an enhanced Bjerknes theory for the case of a liquid subject to weak acoustic forcing. In particular, the equations for the translational velocities of the bubbles were averaged over one cycle of the acoustic forcing to obtain a model that recovers the classical Bjerknes force to leading order and accurately captures the next higher-order terms, cubic in inverse separation distance, which become important for smaller separation distances. Along the way, we showed and made use of the fact that the amplitudes and phases of the radial oscillations depend upon centre-to-centre distance between the bubbles.

This enhanced Bjerknes model contains two key parameters, one of which, called $\mathscr{B}$, arises in standard Bjerknes theory, while the other, $\mathscr{F}$, is directly linked to the nonconstant amplitudes and phases of the radial oscillations. By analysing all four sign combinations of these two key averaging parameters, we were able to classify all of the possible translational motions for two weakly forced bubbles. This analysis predicted the existence of a regime in which there is an unstable equilibrium separation distance, as well as the presence of a regime in which the bubbles exhibit bounded, time-periodic oscillations. Finally, it was also verified that the unaveraged translation equations included the same types of behaviour as the averaged translation equations.

The analysis was continued into the moderately strong forcing regime with the assistance of numerical simulations. We placed particular emphasis on the 2 : 1 resonance zone created by large-amplitude forcing, in which bubbles repel, rather than attract each other as the classical theory predicts. Previous studies have indicated that the pattern of motion for a bubble pair can be dramatically affected by the strength of the acoustic forcing. Our numerical simulations confirmed these observations by showing that bubble pairs can move in directions opposite to that predicted by classical (and enhanced) Bjerknes theory in the presence of strong forcing.

One of the key features of the enhanced Bjerknes theory is that stable bound pair oscillations are observed when the driving frequency is larger than both natural frequencies (i.e. uncoupled Minnaert frequencies). There are two ways to think about how this type of behaviour might be possible. One approach is to focus on the D-dependence of the coupled natural modes. In that case, suppose that the natural frequencies of the bubbles start smaller than the forcing frequency, i.e. $\omega_{N1} < \omega_{N2} < \Omega$. As the bubbles approach each other, the coupled natural frequencies change. In particular, the coupled ω_{N2} increases as D decreases. This may be calculated from the following formula:

$$\omega_{Nj}^2 = \frac{1}{2(1-\epsilon^2)}\left[\omega_{10}^2 + \omega_{20}^2 \pm \sqrt{(\omega_{10}^2 - \omega_{20}^2)^2 + 4\omega_{10}^2\omega_{20}^2\epsilon^2}\right], \quad j = 1, 2, \tag{7.1}$$

where $\epsilon^2 = \epsilon_1\epsilon_2$ and ϵ_j is defined in § 4.2 (see Zabolotskaya 1984 and Appendix C of Harkin 2001). Therefore there exists a possibility that the larger natural frequency can grow to exceed Ω, in which case the natural frequencies will be on opposite sides of the forcing frequency, and hence out of phase. In figure 16(a), we show that $\omega_{N2} - \Omega$

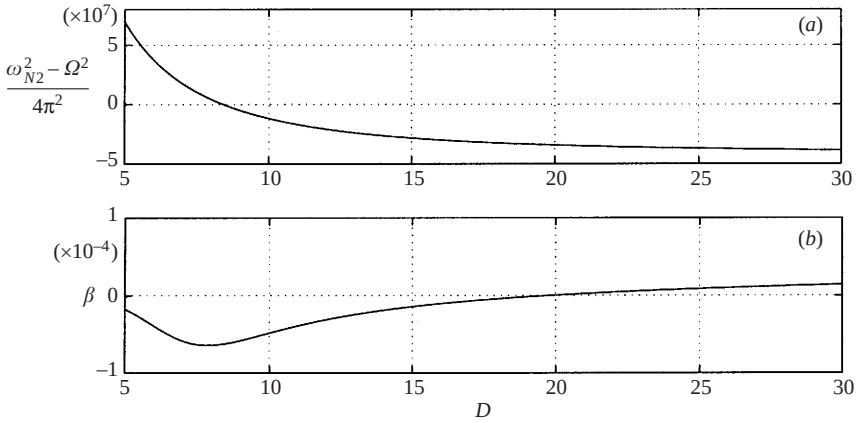

FIGURE 16. (*a*) The natural frequency, ω_{N2}, is plotted versus D using formula (7.1). (*b*) The enhanced Bjerknes theory force parameter, β, is plotted versus D. The parameter values are $R_{10} = 120\,\mu\text{m}$ ($\omega_{10}/2\pi = 27.3\,\text{kHz}$), $R_{20} = 102\,\mu\text{m}$ ($\omega_{20}/2\pi = 32.2\,\text{kHz}$) and $\Omega/2\pi = 32.8\,\text{kHz}$. The D-axis is scaled by R_{10}.

does change sign. For the parameter values shown this occurs near $D = 8$, but as we see in figure 8, the minimum D during the oscillations is approximately 10. Of course, we must keep in mind that the formula for ω_{N2} is only the leading-order formula for large D whereas here D is already relatively small.

A second way is to determine where the sign of the force changes by looking at the coefficient β as in figure 10. In figure 16(*b*), we see that the force between the bubbles changes sign when the parameter β passes through zero, which occurs at approximately $D = 20$, and this agrees qualitatively with the above results for the stable bound pair oscillations.

We thank the anonymous referees for their comments which led to an improvement of the manuscript. We also thank R. G. Holt, G. R. Hall and C. E. Wayne for valuable discussions. The research was partially supported by a Group Infrastructure Grant and a CAREER Grant from the National Science Foundation (DMS-9631755 and DMS-9624471). Also, some of the simulations were run on computing equipment purchased through a SCREMS grant from the NSF (DMS-9977225).

Appendix A. Potential flow and the Weiss sphere theorem

The velocity potential for the flow around two pulsating and translating bubbles is obtained in this Appendix. It is used in § 3 in developing a model for two interacting bubbles.

A.1. *The velocity potential for flow outside two bubbles*

The velocity potential, Φ, for a flow containing two pulsating and translating bubbles consists of two parts,

$$\Phi = \Phi^R + \Phi^T,$$

one part representing the purely radial pulsations of the bubbles, Φ^R, and another part giving the contribution of bubble translation, Φ^T. Moreover, each part can be expanded separately via the method of images:

$$\Phi^R = \Phi_1^R + \Phi_2^R + \Phi_{12}^R + \Phi_{21}^R + \Phi_{121}^R + \Phi_{212}^R + (\text{higher-order image terms})$$

Legendre expansion	Weiss theorem	Legendre expansion	Weiss theorem	Legendre expansion
$\Phi_1^R(r_1,\theta_1)$	$\rightarrow \Phi_1^R(r_2,\theta_2)$	$\rightarrow \Phi_{12}^R(r_2,\theta_2)$	$\rightarrow \Phi_{12}^R(r_1,\theta_1)$	$\rightarrow \Phi_{121}^R(r_1,\theta_1)$ $\rightarrow \Phi_{121}^R(r_2,\theta_2) \rightarrow$
$\Phi_2^R(r_2,\theta_2)$	$\rightarrow \Phi_2^R(r_1,\theta_1)$	$\rightarrow \Phi_{21}^R(r_1,\theta_1)$	$\rightarrow \Phi_{21}^R(r_2,\theta_2)$	$\rightarrow \Phi_{212}^R(r_2,\theta_2) \rightarrow \Phi_{212}^R(r_1,\theta_1) \rightarrow$

TABLE 1. Sequence of calculations involved in the method of images.

and

$$\Phi^T = \Phi_1^T + \Phi_2^T + \Phi_{12}^T + \Phi_{21}^T + \Phi_{121}^T + \Phi_{212}^T + (\text{higher-order image terms}).$$

In the rest of this Appendix, we calculate the individual terms in these expansions. Starting with the velocity potential for an isolated bubble, the calculation consists of two alternating steps. Recall that each bubble possesses a local axisymmetric spherical coordinate system (figure 1). For step one, we perform a Legendre expansion from one local coordinate system to the other. Step two applies the Weiss sphere theorem, which will be explained shortly, to the expanded potential in order to obtain an image potential. With the image potential, we repeat step one, and so forth. This procedure is illustrated in table 1.

A.2. *Contribution from radial pulsations, Φ^R*

We first consider the part of the velocity potential due only to the radial pulsations of the two bubbles. To begin, suppose just bubble 1 is immersed in a quiescent fluid. The velocity potential of the fluid due solely to radial pulsations of bubble 1 is then

$$\Phi_1^R(\vec{r}_1) = -\frac{R_1^2\dot{R}_1}{r_1}. \tag{A 1}$$

Similarly, potential generated by radial pulsations of only bubble 2 would be

$$\Phi_2^R(\vec{r}_2) = -\frac{R_2^2\dot{R}_2}{r_2}. \tag{A 2}$$

To carry out the calculation further we need to be able to transform coordinates from (r_1,θ_1) to (r_2,θ_2) and vice versa (see figure 1). Note from figure 1 that $\vec{r}_2 = \vec{r}_1 - \vec{d}$ where $\vec{d} = (0,0,D)$. Assuming that $R_1 + R_2 \ll D$ we can expand Φ_2^R in the local coordinates of bubble 1 as

$$\Phi_2^R(r_1,\theta_1) = -\frac{R_2^2\dot{R}_2}{|\vec{r}_1 - \vec{d}\,|} = -R_2^2\dot{R}_2\sum_{n=0}^{\infty}\frac{r_1^n}{D^{n+1}}P_n(\cos\theta_1), \tag{A 3}$$

where P_n is the nth Legendre polynomial. Similarly, we have Φ_1^R in the local coordinates of bubble 2,

$$\Phi_1^R(r_2,\theta_2) = -\frac{R_1^2\dot{R}_1}{|\vec{r}_2 + \vec{d}\,|} = -R_1^2\dot{R}_1\sum_{n=0}^{\infty}\frac{(-1)^n r_2^n}{D^{n+1}}P_n(\cos\theta_2). \tag{A 4}$$

Equations (A 1) and (A 2) (or their expansions) are the first terms in the series expansion of the velocity potential, Φ^R, for the flow containing two pulsating bubbles.

The next terms of the series, Φ_{12}^R and Φ_{21}^R, are image terms resulting from these first terms. In order to calculate them, we use a classical result due to Weiss (1944).

A.3. *The Weiss sphere theorem*

THEOREM (Weiss). *If a sphere, S, whose surface is given by $r = a$, is immersed in an arbitrary irrotational flow, then one can write the velocity potential of the new flow as*

$$\Phi = \Phi_u + \Phi_p.$$

Here Φ_u represents the undisturbed flow without the sphere and Φ_p represents the perturbation to the flow caused by the sphere. The latter can be expressed as

$$\Phi_p(\vec{r}\,) = \frac{a}{r}\Phi_u\left(\frac{a^2}{r^2}\vec{r}\right) - \frac{2}{ar}\int_0^a \lambda\Phi_u\left(\frac{\lambda^2}{r^2}\vec{r}\right)\mathrm{d}\lambda.$$

A similar result in two-dimensional potential flow is the well-known circle theorem of Milne-Thompson (1940). As an example of the use of the Weiss theorem, we derive a formula that is needed in subsequent calculations. Consider the flow associated with the undisturbed velocity potential

$$\Phi_u = r^n P_n(\cos\theta).$$

If we insert a sphere of radius R into the flow, the new flow with the sphere derives from the velocity potential $\Phi = \Phi_u + \Phi_p$ and the Weiss sphere theorem gives

$$\begin{aligned}\Phi_p &= \frac{R}{r}\Phi_u\left(\frac{R^2}{r^2}\vec{r}\right) - \frac{2}{Rr}\int_0^R \lambda\Phi_u\left(\frac{\lambda^2}{r^2}\vec{r}\right)\mathrm{d}\lambda \\ &= \frac{R}{r}\left[\frac{R^{2n}}{r^{2n}}r^n P_n(\cos\theta)\right] - \frac{2}{Rr}\int_0^R \lambda\left[\frac{\lambda^{2n}}{r^{2n}}r^n P_n(\cos\theta)\right]\mathrm{d}\lambda \\ &= \frac{n}{n+1}\frac{R^{2n+1}}{r^{n+1}}P_n(\cos\theta). \qquad \text{(A 5)}\end{aligned}$$

A.4. *The image terms Φ_{12}^R and Φ_{21}^R*

The potential Φ_2^R will induce an image 'charge' inside bubble 1 whose potential is Φ_{21}^R. Likewise, the potential Φ_1^R will induce an image charge inside bubble 2 with potential Φ_{12}^R. To obtain the Legendre expansion of these image potentials we apply formula (A 5) term by term to the expansions (A 3) and (A 4). Taking Φ_2^R given by (A 3) to be the undisturbed potential, and taking bubble 1 as the sphere being introduced into the flow, applying formula (A 5) yields

$$\Phi_{21}^R(r_1,\theta_1) = -R_2^2\dot{R}_2\sum_{n=0}^{\infty}\frac{n}{n+1}\frac{R_1^{2n+1}}{r_1^{n+1}D^{n+1}}P_n(\cos\theta_1).$$

Likewise, taking Φ_1^R given by (A 4) to be the undisturbed potential, and inserting bubble 2 into its flow, then formula (A 5) gives

$$\Phi_{12}^R(r_2,\theta_2) = -R_1^2\dot{R}_1\sum_{n=0}^{\infty}\frac{(-1)^n n}{n+1}\frac{R_2^{2n+1}}{r_2^{n+1}D^{n+1}}P_n(\cos\theta_2).$$

Furthermore, upon transforming coordinates again, one may check that

$$\Phi_{21}^R(r_2,\theta_2) = -\frac{R_1^3R_2^2\dot{R}_2}{2D^4} + O\left(\frac{1}{D^5}\right),$$

and

$$\Phi_{12}^R(r_1,\theta_1) = -\frac{R_2^3 R_1^2 \dot{R}_1}{2D^4} + O\left(\frac{1}{D^5}\right).$$

Since $\Phi_{21}^R(r_2,\theta_2)$ and $\Phi_{12}^R(r_1,\theta_1)$ at order D^{-4} do not depend on r or θ then Φ_{121}^R and Φ_{212}^R are both order D^{-5}.

Thus, the part of the two-bubble velocity potential due only to the radial oscillations of the bubbles is

$$\begin{aligned}\Phi^R(r_1,\theta_1) &= \Phi_1^R(r_1,\theta_1) + \Phi_2^R(r_1,\theta_1) + \Phi_{12}^R(r_1,\theta_1) + \Phi_{21}^R(r_1,\theta_1) + \text{h.o.t.}\\ &= -\frac{R_1^2\dot{R}_1}{r_1} - \frac{R_2^2\dot{R}_2}{D} - \frac{R_2^2\dot{R}_2 P_1(\cos\theta_1)}{D^2}\left(r_1 + \frac{R_1^3}{2r_1^2}\right)\\ &\quad - \frac{R_2^2\dot{R}_2 P_2(\cos\theta_1)}{D^3}\left(r_1^2 + \frac{2R_1^5}{3r_1^3}\right) - \frac{R_2^2\dot{R}_2 P_3(\cos\theta_1)}{D^4}\left(r_1^3 + \frac{3R_1^7}{4r_1^4}\right)\\ &\quad - \frac{R_1^3 R_2^2 \dot{R}_2}{2D^4} + O\left(\frac{1}{D^5}\right).\end{aligned}$$

Similarly, in the local coordinates of bubble 2,

$$\begin{aligned}\Phi^R(r_2,\theta_2) &= \Phi_1^R(r_2,\theta_2) + \Phi_2^R(r_2,\theta_2) + \Phi_{12}^R(r_2,\theta_2) + \Phi_{21}^R(r_2,\theta_2) + \text{h.o.t.}\\ &= -\frac{R_2^2\dot{R}_2}{r_2} - \frac{R_1^2\dot{R}_1}{D} + \frac{R_1^2\dot{R}_1 P_1(\cos\theta_2)}{D^2}\left(r_2 + \frac{R_2^3}{2r_2^2}\right)\\ &\quad - \frac{R_1^2\dot{R}_1 P_2(\cos\theta_2)}{D^3}\left(r_2^2 + \frac{2R_2^5}{3r_2^3}\right) + \frac{R_1^2\dot{R}_1 P_3(\cos\theta_2)}{D^4}\left(r_2^3 + \frac{3R_2^7}{4r_2^4}\right)\\ &\quad - \frac{R_2^3 R_1^2 \dot{R}_1}{2D^4} + O\left(\frac{1}{D^5}\right).\end{aligned}$$

A.5. *Contribution from bubble translation, Φ^T*

We now construct the velocity potential for the flow containing two translating bubbles. We begin with the potential representing translation for a single bubble while neglecting the presence of any others,

$$\Phi_1^T(r_1,\theta_1) = -\frac{U_1 R_1^3}{2}\frac{\cos\theta_1}{r_1^2}$$

for bubble 1, and similarly for an isolated bubble 2 we have

$$\Phi_2^T(r_2,\theta_2) = -\frac{U_2 R_2^3}{2}\frac{\cos\theta_2}{r_2^2}.$$

To proceed further, we need expressions for Φ_1^T and Φ_2^T in both local coordinates (i.e. we need $\Phi_1^T(r_2,\theta_2)$ and $\Phi_2^T(r_1,\theta_1)$). To obtain these expressions, first note that $\vec{r}_1 = \vec{r}_2 + \vec{d}$ and $r_1\cos\theta_1 - r_2\cos\theta_2 = D$ (figure 1). As such,

$$\begin{aligned}\Phi_2^T(r_1,\theta_1) &= -\frac{U_2 R_2^3}{2}\frac{(r_1\cos\theta_1 - D)}{|\vec{r}_1 - \vec{d}\,|^3}\\ &= -\frac{U_2 R_2^3}{2}(r_1\cos\theta_1 - D)\left[\sum_{n=0}^{\infty}\frac{r_1^n}{D^{n+1}}P_n(\cos\theta_1)\right]^3\\ &= \frac{U_2 R_2^3}{2D^2} + \frac{U_2 R_2^3}{D^3}r_1 P_1(\cos\theta_1) + \frac{3U_2 R_2^3}{2D^4}r_1^2 P_2(\cos\theta_1) + O\left(\frac{1}{D^5}\right).\end{aligned}$$

Similarly, we have

$$\Phi_1^T(r_2,\theta_2) = -\frac{U_1R_1^3}{2D^2} + \frac{U_1R_1^3}{D^3}r_2P_1(\cos\theta_2) - \frac{3U_1R_1^3}{2D^4}r_2^2P_2(\cos\theta_2) + O\left(\frac{1}{D^5}\right).$$

A.6. *The image terms Φ_{12}^T and Φ_{21}^T*

Again, we employ formula (A 5) to obtain the image terms of Φ_1^T and Φ_2^T. Taking $\Phi_2^T(r_1,\theta_1)$ to be an undisturbed potential into whose flow we insert bubble 1, formula (A 5) gives

$$\Phi_{21}^T(r_1,\theta_1) = \frac{U_2R_2^3}{2D^3}\frac{R_1^3}{r_1^2}P_1(\cos\theta_1) + \frac{U_2R_2^3}{D^4}\frac{R_1^5}{r_1^3}P_2(\cos\theta_1) + O\left(\frac{1}{D^5}\right).$$

Similarly, taking $\Phi_1^T(r_2,\theta_2)$ to be an undisturbed potential into whose flow we insert bubble 2, formula (A 5) yields

$$\Phi_{12}^T(r_2,\theta_2) = \frac{U_1R_1^3}{2D^3}\frac{R_2^3}{r_2^2}P_1(\cos\theta_2) - \frac{U_1R_1^3}{D^4}\frac{R_2^5}{r_2^3}P_2(\cos\theta_2) + O\left(\frac{1}{D^5}\right).$$

One can show that $\Phi_{21}^T(r_2,\theta_2)$ and $\Phi_{12}^T(r_1,\theta_1)$ are of order D^{-5}. Moreover, all higher image terms are also of order D^{-5}. Therefore, the part of the two-bubble velocity potential due only to translation of the bubbles is

$$\begin{aligned}\Phi^T(r_1,\theta_1) &= \Phi_1^T(r_1,\theta_1) + \Phi_2^T(r_1,\theta_1) + \Phi_{12}^T(r_1,\theta_1) + \Phi_{21}^T(r_1,\theta_1) + \text{h.o.t.}\\ &= -\frac{U_1R_1^3}{2}\frac{\cos\theta_1}{r_1^2} + \frac{U_2R_2^3}{2D^2} + \frac{U_2R_2^3P_1(\cos\theta_1)}{D^3}\left(r_1 + \frac{R_1^3}{2r_1^2}\right)\\ &\quad + \frac{U_2R_2^3P_2(\cos\theta_1)}{D^4}\left(\frac{3r_1^2}{2} + \frac{R_1^5}{r_1^3}\right).\end{aligned}$$

Similarly, the translation potential for two bubbles which is valid near bubble 2 is given by

$$\begin{aligned}\Phi^T(r_2,\theta_2) &= \Phi_1^T(r_2,\theta_2) + \Phi_2^T(r_2,\theta_2) + \Phi_{12}^T(r_2,\theta_2) + \Phi_{21}^T(r_2,\theta_2) + \text{h.o.t.}\\ &= -\frac{U_2R_2^3}{2}\frac{\cos\theta_2}{r_2^2} - \frac{U_1R_1^3}{2D^2} + \frac{U_1R_1^3P_1(\cos\theta_2)}{D^3}\left(r_2 + \frac{R_2^3}{2r_2^2}\right)\\ &\quad - \frac{U_1R_1^3P_2(\cos\theta_2)}{D^4}\left(\frac{3r_2^2}{2} + \frac{R_2^5}{r_2^3}\right).\end{aligned}$$

A.7. *The total velocity potential including terms of order D^{-4}*

By combining the above results and noting that $\Phi = \Phi^R + \Phi^T$, the two-bubble velocity potential valid near bubbles 1 and 2 found to be given by expressions (2.1) and (2.2) in § 2.

Appendix B. Derivation of the Oguz–Prosperetti virial theorem

This Appendix is devoted to presenting the proof of the theorem in § 3.1. We highlight the subtle issues that arise due to the fact that, in potential flow, the tangential component of the fluid velocity may differ from that of an interface embedded in the fluid, i.e. slip is allowed at the interface.

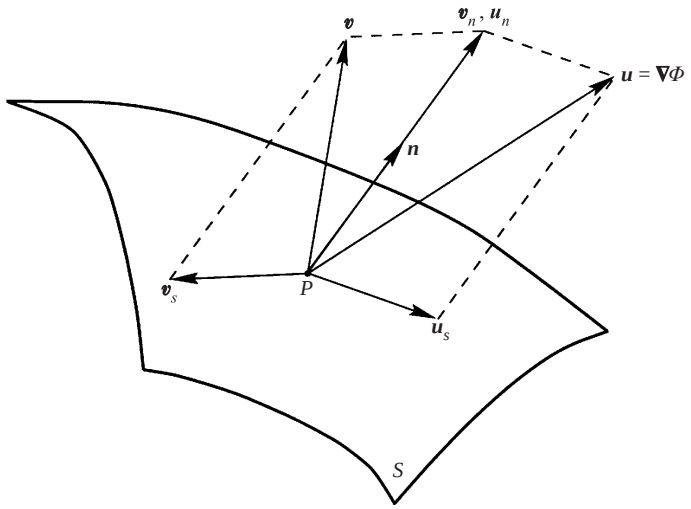

FIGURE 17. Following the fluid versus following the surface.

B.1. *Following the interface versus following the fluid*

Consider the diagram presented in figure 17. Let the velocity vector of a point, P, on the interface, S, be denoted by $\boldsymbol{v}$. Moreover, let the fluid velocity just above the interface be given by $\boldsymbol{u} = \nabla\Phi$. For an inviscid fluid, the boundary condition required at an interface is that the normal component of the interface velocity equals the normal component of the fluid velocity, i.e. $\boldsymbol{n}\cdot\boldsymbol{v} = \boldsymbol{n}\cdot\boldsymbol{u}$. Hence,

$$\begin{aligned}\boldsymbol{v} &= \boldsymbol{v}_s + \boldsymbol{n}(\boldsymbol{n}\cdot\boldsymbol{v})\\ &= \boldsymbol{v}_s + \boldsymbol{n}(\boldsymbol{n}\cdot\boldsymbol{u}) + \boldsymbol{u}_s - \boldsymbol{u}_s\\ &= \boldsymbol{u} + (\boldsymbol{v}_s - \boldsymbol{u}_s),\end{aligned}$$

where $\boldsymbol{v}_s$ and $\boldsymbol{u}_s$ are the components of $\boldsymbol{v}$ and $\boldsymbol{u}$ respectively that lie in the tangent plane to the surface at the point P.

We now adopt the following notation: the substantial derivative with respect to an observer moving with the interface will be given by $\mathrm{d}/\mathrm{d}t \equiv \partial/\partial t + \boldsymbol{v}\cdot\nabla$, whereas $\mathrm{D}/\mathrm{D}t \equiv \partial/\partial t + \boldsymbol{u}\cdot\nabla$ will represent the substantial derivative operator with respect to an observer moving with the fluid flow. Given the previous result relating $\boldsymbol{v}$ and $\boldsymbol{u}$ we see that

$$\frac{\mathrm{d}}{\mathrm{d}t} = \frac{\mathrm{D}}{\mathrm{D}t} + (\boldsymbol{v}_s - \boldsymbol{u}_s)\cdot\nabla_s \tag{B 1}$$

where

$$\nabla_s = (\boldsymbol{I} - \boldsymbol{nn})\cdot\nabla = \nabla - \boldsymbol{n}(\boldsymbol{n}\cdot\nabla).$$

B.2. *Bernoulli's equation*

An important ingredient in the theorem is Bernoulli's equation, which for an inviscid, incompressible fluid undergoing irrotational flow is given by

$$\frac{\mathrm{D}}{\mathrm{D}t}(\Phi) - \tfrac{1}{2}\boldsymbol{u}\cdot\boldsymbol{u} + p' = 0,$$

where

$$p' = \frac{p - p_\infty(t)}{\rho}.$$

We now express Bernoulli's equation with total derivatives that represent an observer moving with the interface S. With the aid of equation (B 1) we find

$$\frac{\mathrm{d}}{\mathrm{d}t}(\Phi) = (\boldsymbol{v}_s - \boldsymbol{u}_s)\cdot\nabla_s\Phi + \tfrac{1}{2}\boldsymbol{u}\cdot\boldsymbol{u} - p'. \tag{B 2}$$

B.3. *Proof of the Oguz–Prosperetti virial theorem*

Let $\boldsymbol{a}$ represent an arbitrary vector field defined on S and apply the surface Reynolds transport theorem (see Nadim 1996 for a recent discussion of these surface theorems) to the integral,

$$\frac{\mathrm{d}}{\mathrm{d}t}\int_{S(t)} \Phi\boldsymbol{a}\cdot\mathrm{d}\boldsymbol{S} = \int_{S(t)} \frac{\mathrm{d}}{\mathrm{d}t}[\Phi\boldsymbol{a}]\cdot\mathrm{d}\boldsymbol{S} + \int_{S(t)} \Phi\boldsymbol{a}\cdot\frac{\mathrm{d}}{\mathrm{d}t}[\mathrm{d}\boldsymbol{S}].$$

Expanding the two terms on the right-hand side and replacing $\mathrm{d}\boldsymbol{S}$ with $\boldsymbol{n}\,\mathrm{d}S$ produces

$$\begin{aligned}\frac{\mathrm{d}}{\mathrm{d}t}\int_{S(t)} \Phi(\boldsymbol{a}\cdot\boldsymbol{n})\,\mathrm{d}\boldsymbol{S} = \int_{S(t)} \left[(\boldsymbol{a}\cdot\boldsymbol{n})\frac{\mathrm{d}}{\mathrm{d}t}(\Phi) + \Phi\boldsymbol{n}\cdot\frac{\mathrm{d}}{\mathrm{d}t}(\boldsymbol{a})\right]\mathrm{d}S \\ + \int_{S(t)} \Phi\boldsymbol{a}\cdot[(\nabla_s\cdot\boldsymbol{v})\boldsymbol{n} - (\nabla_s\boldsymbol{v})\cdot\boldsymbol{n}]\,\mathrm{d}S.\end{aligned}$$

We now substitute equation (B 2) for $(\mathrm{d}/\mathrm{d}t)(\Phi)$ and we use equation (B 1) for $(\mathrm{d}/\mathrm{d}t)(\boldsymbol{a})$. Furthermore, we also replace $\boldsymbol{v}$ with $\boldsymbol{u} + (\boldsymbol{v}_s - \boldsymbol{u}_s)$ which yields

$$\begin{aligned}\frac{\mathrm{d}}{\mathrm{d}t}\int_{S(t)} \Phi(\boldsymbol{a}\cdot\boldsymbol{n})\,\mathrm{d}S = \int_{S(t)} \Bigg[((\boldsymbol{v}_s - \boldsymbol{u}_s)\cdot\nabla_s\Phi + \tfrac{1}{2}\boldsymbol{u}\cdot\boldsymbol{u} - p')(\boldsymbol{a}\cdot\boldsymbol{n}) \\ + \Phi\boldsymbol{n}\cdot\left(\frac{\mathrm{D}}{\mathrm{D}t}(\boldsymbol{a}) + (\boldsymbol{v}_s - \boldsymbol{u}_s)\cdot\nabla_s\boldsymbol{a}\right)\Bigg]\mathrm{d}S \\ + \int_{S(t)} \Phi\boldsymbol{a}\cdot[(\nabla_s\cdot(\boldsymbol{u} + \boldsymbol{v}_s - \boldsymbol{u}_s))\boldsymbol{n} - \nabla_s(\boldsymbol{u} + \boldsymbol{v}_s - \boldsymbol{u}_s)\cdot\boldsymbol{n}]\,\mathrm{d}S.\end{aligned}$$

Expanding the terms on the right-hand side gives

$$\begin{aligned}\frac{\mathrm{d}}{\mathrm{d}t}\int_{S(t)} \Phi(\boldsymbol{a}\cdot\boldsymbol{n})\,\mathrm{d}S = \int_{S(t)} (\boldsymbol{a}\cdot\boldsymbol{n})(\boldsymbol{v}_s - \boldsymbol{u}_s)\cdot\nabla_s\Phi\,\mathrm{d}S + \frac{1}{2}\int_{S(t)} (\boldsymbol{u}\cdot\boldsymbol{u})(\boldsymbol{a}\cdot\boldsymbol{n})\,\mathrm{d}S \\ - \int_{S(t)} p'(\boldsymbol{a}\cdot\boldsymbol{n})\,\mathrm{d}S + \int_{S(t)} \Phi\boldsymbol{n}\cdot\frac{\mathrm{D}}{\mathrm{D}t}(\boldsymbol{a})\,\mathrm{d}S \\ + \int_{S(t)} \Phi(\boldsymbol{v}_s - \boldsymbol{u}_s)\cdot(\nabla_s\boldsymbol{a})\cdot\boldsymbol{n}\,\mathrm{d}S + \int_{S(t)} \Phi(\boldsymbol{a}\cdot\boldsymbol{n})(\nabla\cdot\boldsymbol{u})\,\mathrm{d}S \\ + \int_{S(t)} \Phi(\boldsymbol{a}\cdot\boldsymbol{n})(\nabla_s\cdot(\boldsymbol{v}_s - \boldsymbol{u}_s))\,\mathrm{d}S - \int_{S(t)} \Phi\boldsymbol{a}\cdot(\nabla\boldsymbol{u})\cdot\boldsymbol{n}\,\mathrm{d}S \\ - \int_{S(t)} \Phi\boldsymbol{a}\cdot(\nabla_s(\boldsymbol{v}_s - \boldsymbol{u}_s))\cdot\boldsymbol{n}\,\mathrm{d}S.\end{aligned}$$

The ∇_s in the sixth and the eighth terms on the right-hand side were replaced with the full ∇ because it can be shown that

$$(\boldsymbol{a}\cdot\boldsymbol{n})(\nabla\cdot\boldsymbol{u}) - \boldsymbol{a}\cdot(\nabla\boldsymbol{u})\cdot\boldsymbol{n} = (\boldsymbol{a}\cdot\boldsymbol{n})(\nabla_s\cdot\boldsymbol{u}) - \boldsymbol{a}\cdot(\nabla_s\boldsymbol{u})\cdot\boldsymbol{n}.$$

Next let $\boldsymbol{w} = \boldsymbol{v}_s - \boldsymbol{u}_s$ and recall that $\nabla \cdot \boldsymbol{u} = 0$. After rearranging the order of the terms we get

$$\begin{aligned}\frac{\mathrm{d}}{\mathrm{d}t}\int_{S(t)} \Phi(\boldsymbol{a}\cdot\boldsymbol{n})\,\mathrm{d}S = \int_{S(t)} \Phi\left[\boldsymbol{n}\cdot\frac{\mathrm{D}}{\mathrm{D}t}(\boldsymbol{a}) - \boldsymbol{a}\cdot(\nabla\boldsymbol{u})\cdot\boldsymbol{n}\right]\mathrm{d}S + \frac{1}{2}\int_{S(t)}(\boldsymbol{u}\cdot\boldsymbol{u})(\boldsymbol{a}\cdot\boldsymbol{n})\,\mathrm{d}S \\ - \int_{S(t)} p'(\boldsymbol{a}\cdot\boldsymbol{n})\,\mathrm{d}S + \int_{S(t)}(\boldsymbol{a}\cdot\boldsymbol{n})\boldsymbol{w}\cdot\nabla_s\Phi\,\mathrm{d}S \\ + \int_{S(t)} \Phi\boldsymbol{w}\cdot(\nabla_s\boldsymbol{a})\cdot\boldsymbol{n}\,\mathrm{d}S + \int_{S(t)}\Phi(\boldsymbol{a}\cdot\boldsymbol{n})(\nabla_s\cdot\boldsymbol{w})\,\mathrm{d}S \\ - \int_{S(t)} \Phi\boldsymbol{a}\cdot(\nabla_s\boldsymbol{w})\cdot\boldsymbol{n}\,\mathrm{d}S. \qquad \text{(B 3)}\end{aligned}$$

To arrive at the refined Oguz–Prosperetti theorem we see that the sum of the last four integrals on the right-hand side must vanish. Hence, we must have

$$\int_{S(t)} [(\boldsymbol{a}\cdot\boldsymbol{n})\boldsymbol{w}\cdot\nabla_s\Phi + \Phi\boldsymbol{w}\cdot(\nabla_s\boldsymbol{a})\cdot\boldsymbol{n} + \Phi(\boldsymbol{a}\cdot\boldsymbol{n})(\nabla_s\cdot\boldsymbol{w}) - \Phi\boldsymbol{a}\cdot(\nabla_s\boldsymbol{w})\cdot\boldsymbol{n}]\,\mathrm{d}S = 0.$$

Under what conditions is this expression equal to zero? If a no-slip condition is imposed at the interface then $\boldsymbol{w} = \boldsymbol{v}_s - \boldsymbol{u}_s = \boldsymbol{0}$ and each of the four terms vanishes. Alternatively, if tangential slip is allowed at the interface then $\boldsymbol{w} \neq \boldsymbol{0}$, and to answer the question we note the following:

$$\begin{aligned}\int_{S(t)} [(\boldsymbol{a}\cdot\boldsymbol{n})\boldsymbol{w}\cdot\nabla_s\Phi + \Phi\boldsymbol{w}\cdot(\nabla_s\boldsymbol{a})\cdot\boldsymbol{n} + \Phi(\boldsymbol{a}\cdot\boldsymbol{n})(\nabla_s\cdot\boldsymbol{w}) - \Phi\boldsymbol{a}\cdot(\nabla_s\boldsymbol{w})\cdot\boldsymbol{n}]\,\mathrm{d}S \\ = \int_{S(t)} \nabla_s\cdot[\Phi(\boldsymbol{a}\cdot\boldsymbol{n})\boldsymbol{w}]\,\mathrm{d}S - \int_{S(t)} \Phi\boldsymbol{w}\cdot(\nabla_s\boldsymbol{n})\cdot\boldsymbol{a}\,\mathrm{d}S - \int_{S(t)} \Phi\boldsymbol{a}\cdot(\nabla_s\boldsymbol{w})\cdot\boldsymbol{n}\,\mathrm{d}S.\end{aligned}$$

For a closed surface, S, the first integral on the right-hand side is identically equal to zero by the surface divergence theorem (Nadim 1996). Moreover, if $\boldsymbol{a} = f\boldsymbol{n}$ where $f : S \to \mathbb{R}$ then the last two terms on the right-hand side also vanish identically because

$$\begin{aligned}&\text{(i)}\ \ (\nabla_s\boldsymbol{n})\cdot\boldsymbol{n} = \tfrac{1}{2}\nabla_s(\boldsymbol{n}\cdot\boldsymbol{n}) = 0,\\ &\text{(ii)}\ \ \boldsymbol{n}\cdot\nabla_s = 0.\end{aligned}$$

So if $\boldsymbol{a} = f\boldsymbol{n}$ then no input concerning the relative tangential velocity of the interface is required in order to use the Oguz–Prosperetti virial theorem. In other words, while Oguz & Prosperetti allow $\boldsymbol{a}$ to be an arbitrary vector field, we find that it must be of the form $\boldsymbol{a} = f\boldsymbol{n}$ in order to make the result independent of whether or not the tangential velocities of the fluid and the interface are the same. Equation (3.1) is obtained from taking $\boldsymbol{a} = f\boldsymbol{n}$ in (B 3).

Appendix C. Alternative derivation of the equations of motion

In this Appendix, we calculate the pressure in the liquid outside two pulsating and translating bubbles. Averaging the liquid pressure on the bubble surfaces yields the equations governing the radii of each bubble. Moreover, by using the liquid pressure to obtain the force on each bubble, we can also obtain the translation equations for the bubble centres.

Bernoulli's equation for the pressure in the fluid is

$$\frac{p_{\mathrm{L}} - p_\infty(t)}{\rho} = -\left(\frac{\partial \Phi}{\partial t}\right)_{\vec{x}} - \tfrac{1}{2}\|\nabla_{\vec{x}}\,\Phi\|^2, \tag{C 1}$$

where $\vec{x}$ denotes fixed laboratory coordinates. Since the local bubble coordinates are in motion relative to the fixed laboratory coordinates, the derivatives transform according to

$$\nabla_{\vec{x}} = \nabla_{\vec{r}}, \qquad \left(\frac{\partial}{\partial t}\right)_{\vec{x}} = \left(\frac{\partial}{\partial t}\right)_{\vec{r}} - \boldsymbol{U}\cdot\nabla_{\vec{r}}.$$

By substituting the two-bubble potential $\Phi(r_1, \theta_1)$ into Bernoulli's equation (C 1), and evaluating at $r = R_1$, we obtain an expansion for the liquid pressure at the surface of bubble 1:

$$\begin{aligned} p_1' = {} & R_1\ddot{R}_1 + \tfrac{3}{2}\dot{R}_1^2 + \frac{2R_2\dot{R}_2^2 + R_2^2\ddot{R}_2}{D} - \frac{R_2^2\dot{R}_2(3U_1 + 3U_2 + 2\dot{D}) + R_2^3\dot{U}_2}{2D^2} - \frac{U_1^2}{4} \\ & + \tfrac{1}{2}P_1(\cos\theta)\left[R_1\dot{U}_1 + 3\dot{R}_1U_1 + \frac{3R_1R_2^2\ddot{R}_2 + 6R_1R_2\dot{R}_2^2 + 3R_2^2\dot{R}_1\dot{R}_2}{D^2}\right] \\ & + P_2(\cos\theta)\left[\tfrac{3}{4}U_1^2 + \frac{3R_2^2\dot{R}_2U_1}{2D^2}\right] + O\left(\frac{1}{D^3}\right). \end{aligned} \tag{C 2}$$

The average of p_1' over the surface of bubble 1 is just the first line of (C 2), which leads to exactly the same radial equation as in § 3.2 (note that the averages of $P_1(\cos\theta)$ and $P_2(\cos\theta)$ vanish).

Next, the force on each bubble is given by $\boldsymbol{F} = -\int_S p_{\mathrm{L}}\boldsymbol{n}\,\mathrm{d}S$ where the integral is over the surface of the bubble and $\boldsymbol{n}$ is the outward unit normal to the bubble surface. In the local bubble coordinates we can express this force as

$$\boldsymbol{F} = -\int_0^{2\pi}\int_0^{\pi} p_{\mathrm{L}}\hat{\boldsymbol{e}}_r R^2 \sin\theta\,\mathrm{d}\theta\,\mathrm{d}\phi.$$

The component of this force, F_z, directed along the line connecting the centres of the bubbles (F_z is the projection of $\boldsymbol{F}$ onto $\boldsymbol{d} = D\hat{\boldsymbol{k}}$) is given by

$$F_z = -2\pi R^2\int_0^{\pi} p_{\mathrm{L}}\cos\theta\sin\theta\,\mathrm{d}\theta = -\pi R^2\int_0^{\pi} p_{\mathrm{L}}\sin(2\theta)\,\mathrm{d}\theta.$$

Employing expression (C 2) for the pressure we can calculate the force on bubble 1:

$$F_z = -2\pi\rho\left[\frac{\mathrm{d}}{\mathrm{d}t}\left(\frac{R_1^3U_1}{3} + \frac{R_1^3R_2^2\dot{R}_2}{D^2}\right) - \frac{2R_1^2\dot{R}_1R_2^2\dot{R}_2}{D^2}\right],$$

where terms of order D^{-2} have been kept. This expression for the force on a bubble is in fact in agreement with the translation equations derived in § 3.3, for if we let ρ_g represent the density of the gas inside the bubble, then

$$\frac{\mathrm{d}}{\mathrm{d}t}(\tfrac{4}{3}\pi R_1^3\rho_g U_1) = F_z$$

governs the motion of the bubble. But since $\rho_g/\rho \ll 1$ the motion of the bubble is approximated well by $F_z \approx 0$, which exactly yields the translation equation (3.7). The forces acting on a pulsating and translating bubble in a potential flow have also been examined by Lhuillier (1982), see also Nigmatulin (1991).

Appendix D. Calculation of the averaging parameters β and γ

D.1. *Calculation of* β

Let $W_j = \omega_{j0}^2 - \Omega^2$ for $j = 1, 2$ and recall that

$$X_1 = \frac{(W_2 + \mathrm{i}\Omega\zeta_2)P_1 + \epsilon_1\Omega^2 P_2}{(W_1 + \mathrm{i}\Omega\zeta_1)(W_2 + \mathrm{i}\Omega\zeta_2) - \epsilon_1\epsilon_2\Omega^4} = \frac{z_1}{Q} = \frac{\|z_1\|\,\mathrm{e}^{\mathrm{i}\theta_1}}{\|Q\|\,\mathrm{e}^{\mathrm{i}\alpha}} = \frac{\|z_1\|}{\|Q\|}\,\mathrm{e}^{\mathrm{i}(\theta_1-\alpha)} = \delta_1\,\mathrm{e}^{\mathrm{i}\psi_1}$$

and

$$X_2 = \frac{(W_1 + \mathrm{i}\Omega\zeta_1)P_2 + \epsilon_2\Omega^2 P_1}{(W_1 + \mathrm{i}\Omega\zeta_1)(W_2 + \mathrm{i}\Omega\zeta_2) - \epsilon_1\epsilon_2\Omega^4} = \frac{z_2}{Q} = \frac{\|z_2\|\,\mathrm{e}^{\mathrm{i}\theta_2}}{\|Q\|\,\mathrm{e}^{\mathrm{i}\alpha}} = \frac{\|z_2\|}{\|Q\|}\,\mathrm{e}^{\mathrm{i}(\theta_2-\alpha)} = \delta_2\,\mathrm{e}^{\mathrm{i}\psi_2}.$$

Note that $\psi_1 - \psi_2 = (\theta_1 - \alpha) - (\theta_2 - \alpha) = \theta_1 - \theta_2$. Hence,

$$\begin{aligned}
\beta &= 2\pi\rho\Omega^2 R_{10}^3 R_{20}^3 \delta_1\delta_2 \cos(\psi_1 - \psi_2)\\
&= 2\pi\rho\Omega^2 R_{10}^3 R_{20}^3 \delta_1\delta_2 \cos(\theta_1 - \theta_2)\\
&= 2\pi\rho\Omega^2 R_{10}^3 R_{20}^3 \delta_1\delta_2 (\cos\theta_1\cos\theta_2 + \sin\theta_1\sin\theta_2)\\
&= 2\pi\rho\Omega^2 R_{10}^3 R_{20}^3 \frac{\|z_1\|}{\|Q\|}\frac{\|z_2\|}{\|Q\|}\left(\frac{\mathrm{Re}(z_1)}{\|z_1\|}\frac{\mathrm{Re}(z_2)}{\|z_2\|} + \frac{\mathrm{Im}(z_1)}{\|z_1\|}\frac{\mathrm{Im}(z_2)}{\|z_2\|}\right)\\
&= 2\pi\rho\Omega^2 R_{10}^3 R_{20}^3 \left(\frac{\mathrm{Re}(z_1)\,\mathrm{Re}(z_2) + \mathrm{Im}(z_1)\,\mathrm{Im}(z_2)}{\|Q\|^2}\right)\\
&= 2\pi\rho\Omega^2 R_{10}^3 R_{20}^3 \frac{(W_2P_1 + \epsilon_1\Omega^2P_2)(W_1P_2 + \epsilon_2\Omega^2P_1) + \Omega^2 P_1P_2\zeta_1\zeta_2}{(W_1W_2 - \Omega^2\zeta_1\zeta_2 - \epsilon_1\epsilon_2\Omega^4)^2 + (W_1\Omega\zeta_2 + W_2\Omega\zeta_1)^2}.
\end{aligned}$$

Recall that ϵ_1 and ϵ_2 depend on D via (4.7).

D.2. *Calculation of* γ

Following the same line of reasoning as above we obtain

$$\begin{aligned}
\gamma &= 3\pi\rho\Omega R_{10}^3 R_{20}^3 \delta_1\delta_2 \sin(\psi_1 - \psi_2)\\
&= 3\pi\rho\Omega R_{10}^3 R_{20}^3 \delta_1\delta_2 \sin(\theta_1 - \theta_2)\\
&= 3\pi\rho\Omega R_{10}^3 R_{20}^3 \delta_1\delta_2 (\sin\theta_1\cos\theta_2 - \sin\theta_2\cos\theta_1)\\
&= 3\pi\rho\Omega R_{10}^3 R_{20}^3 \frac{\|z_1\|}{\|Q\|}\frac{\|z_2\|}{\|Q\|}\left(\frac{\mathrm{Im}(z_1)}{\|z_1\|}\frac{\mathrm{Re}(z_2)}{\|z_2\|} - \frac{\mathrm{Im}(z_2)}{\|z_2\|}\frac{\mathrm{Re}(z_1)}{\|z_1\|}\right)\\
&= 3\pi\rho\Omega R_{10}^3 R_{20}^3 \left(\frac{\mathrm{Im}(z_1)\,\mathrm{Re}(z_2) - \mathrm{Im}(z_2)\,\mathrm{Re}(z_1)}{\|Q\|^2}\right)\\
&= 3\pi\rho\Omega R_{10}^3 R_{20}^3 \frac{\Omega\zeta_2P_1(W_1P_2 + \epsilon_2\Omega^2P_1) - \Omega\zeta_1P_2(W_2P_1 + \epsilon_1\Omega^2P_2)}{(W_1W_2 - \Omega^2\zeta_1\zeta_2 - \epsilon_1\epsilon_2\Omega^4)^2 + (W_1\Omega\zeta_2 + W_2\Omega\zeta_1)^2}.
\end{aligned}$$

REFERENCES

Barbat, T., Ashgriz, N. & Liu, C. S. 1999 Dynamics of two interacting bubbles in an acoustic field. *J. Fluid Mech.* **389**, 137–168.

Bjerknes, C. A. 1915 *Hydrodynamische Fernkrafte.* Engelmann, Leipzig.

Bjerknes, V. F. K. 1906 *Fields of Force.* Columbia University Press.

Crum, L. A. 1975 Bjerknes forces on bubbles in a stationary sound field. *J. Acoust. Soc. Am.* **57**, 1363–1370.

Doinikov, A. A. 1997*a* Acoustic radiation force on a spherical particle in a viscous heat-conducting fluid. I. General formula. *J. Acoust. Soc. Am.* **101**, 713–721.

Doinikov, A. A. 1997*b* Dissipative effects on Bjerknes forces between two bubbles. *J. Acoust. Soc. Am.* **102**, 747–751.

Doinikov, A. A. 1999 Effects of the second harmonic on the secondary Bjerknes force. *Phys. Rev.* E **59**, 3016–3021.

Doinikov, A. A. & Zavtrak, S. T. 1995 On the mutual interaction of two gas bubbles in a sound field. *Phys. Fluids* **7**, 1923–1930.

Doinikov, A. A. & Zavtrak, S. T. 1997 Radiation forces between two bubbles in a compressible liquid. *J. Acoust. Soc. Am.* **102**, 1424–1430.

Fujikawa, S. & Takahira, H. 1986 A theoretical study on the interaction between two spherical bubbles and radiated pressure waves in a liquid. *Acustica* **61**, 188–199.

Harkin, A. 2001 Nonlinear dynamics of gas bubbles in liquids. PhD Thesis, Boston University.

Leal, L. G. 1992 *Laminar Flow and Convective Transport Processes.* Butterworth-Heinemann.

Leighton, T. G. 1994 *The Acoustic Bubble.* Academic.

Lhuillier, D. 1982 Forces d'inertie sur une bulle en expansion se deplacant dans un fluid. *C. R. Acad. Sci. Paris* II **295**, 95–98.

Magnaudet, J. & Eames, I. 2000 The motion of high-Reynolds-number bubbles in inhomogeneous flows. *Ann. Rev. Fluid Mech.* **32**, 659–708.

Mettin, R., Akhatov, I., Parlitz, U., Ohl, C. D. & Lauterborn, W. 1997 Bjerknes forces between small cavitation bubbles in a strong acoustic field. *Phys. Rev.* E **56**, 2924–2931.

Milne-Thomson, L. M. 1940 Hydrodynamical images. *Proc. Camb. Phil. Soc.* **36**, 246–247.

Minnaert, M. 1933 On the musical air bubbles and the sound of running water. *Phil. Mag.* **16**, 235–248.

Nadim, A. 1996 A concise introduction to surface rheology with application to dilute emulsions of viscous drops. *Chem. Engng Commun.* **148–150**, 391–407.

Nigmatulin, R. I. 1991 *Dynamics of Multiphase Media*, Vols. 1 and 2. Hemisphere.

Oguz, H. N. & Prosperetti, A. 1990 A generalization of the impulse and virial theorems with an application to bubble oscillations. *J. Fluid Mech.* **218**, 143–162.

Pelekasis, N. A. 1991 A study on drop and bubble dynamics via a hybrid boundary element-finite element methodology. PhD Thesis, SUNY Buffalo.

Pelekasis, N. A. & Tsamopoulos, J. A. 1993*a* Bjerknes forces between two bubbles. Part 1. Response to a step change in pressure. *J. Fluid Mech.* **254**, 467–499.

Pelekasis, N. A. & Tsamopoulos, J. A. 1993*b* Bjerknes forces between two bubbles. Part 2. Response to an oscillatory pressure field. *J. Fluid Mech.* **254**, 501–527.

Plesset, M. S. & Prosperetti, A. 1977 Bubble dynamics and cavitation. *Ann. Rev. Fluid Mech.* **9**, 145–185.

Takahira, H., Fujikawa, S. & Akamatsu, T. 1989 Numerical investigation of nonlinear oscillations of two spherical gas bubbles in a compressible liquid. *JSME Intl J.* II **32**, 163–172.

Weiss, P. 1944 On hydrodynamical images: arbitrary irrotational flow disturbed by a sphere. *Proc. Camb. Phil. Soc.* **40**, 259–261.

Zabolotskaya, E. A. 1984 Interaction of gas bubbles in a sound field. *Sov. Phys. Acoust.* **30**, 365–368.